Spatiotemporally Resolved Ion Velocity Distribution Measurements in the 12.5 kW HERMeS Hall Thruster

IEPC-2019-532

Presented at the 36th International Electric Propulsion Conference
University of Vienna, Austria
September 15-20, 2019

Vernon H. Chaplin,[*] Robert B. Lobbia,[†] Alejandro Lopez Ortega,[‡] Ioannis G. Mikellides,[§]
Parker J. Roberts,[¶] Jonah S. Peter,[‖] Richard R. Hofer,[**] James E. Polk,[††]
Jet Propulsion Laboratory, California Institute of Technology, Pasadena, CA 91109, USA

and

Adam J. Friss[‡‡]
Colorado State University, Fort Collins, CO 80523, USA

We present time-averaged and time-resolved laser-induced fluorescence (LIF) measurements of xenon ion velocities carried out to support life modeling of the 12.5 kW Hall Effect Rocket with Magnetic Shielding (HERMeS) with the Hall2De code. High resolution time-averaged velocity vector maps were constructed to enable detailed validation of the simulated ion velocities and plasma potentials in regions of importance for life-limiting erosion of the front pole and cathode keeper. At the 300 V operating conditions that have exhibited unexpectedly high inner pole erosion, greater radial divergence of the ion trajectories in the beam edges was observed at 1.25 times the nominal magnetic field strength than at lower fields, consistent with inner pole erosion trends. A procedure was developed for quantifying the random uncertainty in mean velocities calculated from noisy LIF data, and the method was applied to comparisons of LIF results obtained on HERMeS thrusters in two different facilities. Measurements in the cathode plume of the operating thruster revealed mean velocities primarily in the positive radial direction, with a large ($>$ 10 eV) energy spread far from the cathode centerline. Time-resolved LIF (TRLIF) was implemented using the transfer function averaging method, enabling study of both periodic and aperiodic oscillation regimes with a measurement bandwidth of $\sim$ 100 kHz. The measurements produced direct confirmation of rapid acceleration zone movement during large-amplitude discharge current oscillations at the 500–600 V operating conditions, and $\gtrsim$ 100 V peak-to-peak oscillations in the near plume plasma potential were also detected at these conditions. Non-negligible acceleration zone movement and beam edge velocity vector time dependence were also measured at the 300–400 V operating conditions, but these smaller amplitude oscillations appeared to be unlikely to have a dramatic effect on pole erosion.

[*]Technologist, Electric Propulsion Group, vernon.h.chaplin@jpl.nasa.gov
[†]Technologist, Electric Propulsion Group, robert.b.lobbia@jpl.nasa.gov
[‡]Member of the Technical Staff, Electric Propulsion Group, alejandro.lopez.ortega@jpl.nasa.gov
[§]Principal Engineer, Electric Propulsion Group, ioannis.g.mikellides@jpl.nasa.gov
[¶]Student Intern, Electric Propulsion Group, parker.roberts@vikings.berry.edu
[‖]Contractor, Electric Propulsion Group, jonah.s.peter@jpl.nasa.gov
[**]Supervisor, Electric Propulsion Group, richard.r.hofer@jpl.nasa.gov
[††]Principal Engineer, Propulsion and Materials Engineering Section, james.e.polk@jpl.nasa.gov
[‡‡]PhD, Department of Mechanical Engineering, Adam.Friss@colostate.edu

Nomenclature

GRC	= Glenn Research Center
JPL	= Jet Propulsion Laboratory
HERMeS	= Hall Effect Rocket with Magnetic Shielding
AEPS	= Advanced Electric Propulsion System
LIF	= Laser-induced fluorescence
TRLIF	= Time-resolved laser-induced fluorescence
r, z	= Radial and axial position coordinates
v	= Velocity
IVDF	= Ion velocity distribution function
$f(v)$	= Ion velocity distribution function
ETU	= Engineering model thruster
TDU	= Technology Development model thruster
V_d	= Discharge voltage
B	= Magnetic field magnitude
$B_{nom.}$	= Nominal magnetic field strength setting for HERMeS
P_{BG}	= Background pressure
MS	= Magnetically shielded
LaB_6	= Lanthanum hexaboride
I_d	= Discharge current
Xe II	= Singly ionized xenon
AOM	= Acousto-optic modulator
IR	= Infrared
SNR	= Signal-to-noise ratio
σ	= Standard deviation
α	= Velocity vector angle
$L_{channel}$	= Discharge channel length (reference length for normalization)
ϕ	= Plasma potential
k_B	= Boltzmann's constant
T_e	= Electron temperature
e	= Electron charge
n_e	= Electron density
u	= Mean velocity
ΔE	= Ion energy spread
M_i	= Xenon ion mass
f	= Frequency
ω	= Angular frequency
$\hat{l}(\omega)$	= Fourier transform of the LIF signal at one laser wavelength
$H(\omega)$	= Transfer function
$\hat{r}(\omega)$	= Fourier transform of the reference signal for transfer function averaging
t	= time
V_{cg}	= Cathode-to-ground voltage
PMT	= Photomultiplier tube
DC	= Direct current / Signal component at $f = 0$
τ_{PSD}	= Low-pass filter time constant for phase-sensitive detection
f_{signal}	= LIF signal frequency
f_{mod}	= Laser modulation frequency
f_{DAQ}	= Data sampling frequency

I. Introduction

After a successful technology maturation program at NASA Glenn Research Center (GRC) and Jet Propulsion Laboratory (JPL), the 12.5 kW Hall Effect Rocket with Magnetic Shielding (HERMeS) is being developed for flight as part of the Advanced Electric Propulsion System (AEPS) under a contract with Aerojet Rocketdyne. Life qualification of the thruster[1,2] will be accomplished through a combination of long-duration wear tests at GRC and computational modeling using JPL's Hall2De code.[3–5] Laser-induced fluorescence (LIF) measurements[6–8] are playing an important role in the modeling effort, providing necessary data to determine the anomalous electron transport profile in the vicinity of the acceleration region[8–10] and allowing for detailed validation of the plasma models through comparisons of measured and simulated ion velocity vectors.[4,11]

Previous LIF campaigns at JPL[8,12] and GRC[13] focused on providing the baseline data required for model validation and demonstrating an LIF capability applicable to testing of Engineering Model (ETU) thrusters that will be delivered to NASA by Aerojet in 2019. Key findings included trends in acceleration zone location and shape as a function of discharge voltage (V_d), magnetic field strength (B), and background pressure (P_{BG}),[8,12] measurements of ion velocity distributions in front of the magnetic poles,[13] and evidence for back-and-forth motion of the acceleration region during global discharge oscillations.[8,12] Hall2De simulations showed that at higher voltage operating conditions (V_d = 500–600 V), these oscillations could dramatically increase front pole erosion,[4] which is likely to be the most important life limiting mechanism for HERMeS[4,14,15] due to the elimination of significant discharge channel erosion in magnetically shielded (MS) thrusters.[16–18]

As of 2018, the Hall2De simulations had been successful in reproducing and explaining the measured pole erosion rates[19,20] in HERMeS at high V_d,[4] but complete understanding of the elevated erosion rates at V_d = 300 V, along with details of other erosion trends such as scaling with magnetic field strength, remained elusive. Therefore, additional LIF measurements were carried out at JPL to further inform the models. The focus was on obtaining high spatial and temporal resolution in regions thought to be of particular importance for pole erosion, in order to more precisely validate the existing simulation features and to aid identification of missing physics that could help explain the erosion data over the full range of operating conditions. In particular, three main goals were identified:

- **Carry out time-resolved LIF (TRLIF) measurements.** The primary objective was to verify the interpretation advanced in Refs. 8 and 12 that the bi-modal time-averaged ion velocity distributions (IVDFs) observed in the acceleration region at V_d = 500–600 V were caused by oscillations in the acceleration region position, and to characterize the time dependence in detail. A second objective was to look for oscillations in the beam edges that could enhance pole erosion at V_d = 300 V. In order to accomplish these goals, the TRLIF technique was required to have bandwidth $\geq$ 55 kHz (in order to resolve the fundamental frequency of the nearly periodic discharge oscillations at 500–600 V), and it also needed to be able to handle the aperiodic oscillations at 300–400 V.[8,12] Therefore, we employed the transfer functioning averaging technique developed by Lobbia and Durot,[21–23] which averages over many data acquisitions using an assumed linear relationship in Fourier space between the LIF signal and a reference signal such as discharge current, and therefore does not require nearly periodic oscillations like other TRLIF approaches.[24–30]

- **Construct time-averaged ion velocity vector maps with high spatial resolution in the channel and beam edges.** These measurements sought to resolve ambiguity in the details of plasma potential contours that remained after analysis of more coarsely spaced LIF vector maps.[11,13]

- **Measure time-averaged IVDFs along two axes in the cathode plume during thruster operation**. These were the first LIF data obtained near the centrally mounted HERMeS cathode, enabling validation of the plasma model in this region and providing information about energies of ions that could contribute to inner pole and cathode keeper erosion.

This paper presents an overview of results from this experimental campaign. Sec. II provides background information on the thruster tested and the LIF setup. Sec. III presents results of the time-averaged LIF measurements and discusses an approach for quantifying uncertainties in mean velocities calculated from noisy velocity distributions. Sec. IV explains the TRLIF hardware and data processing techniques, describes validation experiments carried out to provide confidence that the analyses were producing reliable results,

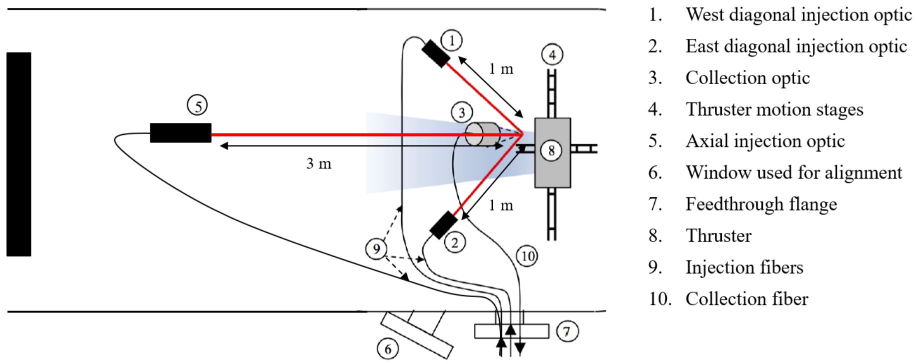

Figure 1. Schematic of the in-chamber optics arrangement for LIF measurements on HERMeS TDU-2.

and presents time-resolved IVDFs and mean velocities measured in HERMeS at V_d = 300, 400, 500, and 600 V. Conclusions are presented in Sec. V.

II. Experimental Setup

A. Thruster and Facility

The HERMeS thruster tested was the NASA-built Technology Demonstration Unit 2 (TDU-2), the same thruster used for previously for LIF measurements,[8,12] erosion measurements,[20] and environmental testing[31] at JPL. A center-mounted[32] lanthanum hexaboride (LaB_6) hollow cathode[33] was used, and the thruster body was electrically tied to cathode common.[34]

Testing took place in the JPL Owens Chamber facility, a $\sim$ 3 m diameter, $\sim$ 10 m long cryogenically-pumped chamber lined with graphite. The background pressure measured by a xenon-calibrated Stabil ion gauge mounted in the thruster exit plane was between 10–13 μTorr during the collection of all data presented in this paper, with the exception of the channel centerline TRLIF dataset at V_d = 600 V, I_d = 20.8 A, which was acquired at pressures as high as 14.2 μTorr.

B. LIF Setup

We employed the common LIF scheme for singly-ionized xenon (Xe II) targeting the 834.953 nm (vacuum wavelength) transition out of the $5p^4\left({}^3P_2\right)5d^2\,[4]_{7/2}$ metastable state, with fluorescence detected at 542.06 nm. The output of a 500 mW amplified tunable diode laser was split along multiple beam paths and fiber-coupled into the vacuum chamber—by scanning the laser wavelength such that the Doppler-shifted laser photons could interact with ions with different velocity components along the beam direction, the IVDF was mapped out.

A diagram of the LIF setup[8,12,14,35] is shown in Fig. 1. One injection optic was mounted directly downstream of the thruster in order to measure the axial IVDF; the lens assembly was shielded from the ion beam by a water-cooled graphite panel with an embedded borosilicate window. Two additional injection optics, labeled "East" and "West" in the figure, were offset 45 degrees from the axial and radial directions—these were used to measure mean velocity vectors both inside and exterior to the discharge channel. The collection optic was mounted above the thruster, approximately 70 degrees out of the plane containing the injection beams (i.e., the thruster's vertical midplane).

The laser beams were chopped using acousto-optic modulators (AOMs). For time-averaged LIF, commercial lock-in amplifiers were used to extract the desired signals from the noise (which was dominated by background light emission from other regions of the plasma), and data could be taken along two lines of sight simultaneously. For time-resolved LIF, chopping frequencies on the order of 1 MHz were employed, and lock-in amplification was accomplished in post-processing, as described in Sec. IV.

The axial injection beam was π-polarized (i.e., the laser beam electric field was approximately aligned with the thruster's radial magnetic field) in order to minimize Zeeman splitting for an accurate measurement of the width of the time-resolved axial IVDFs.[36] The diagonal injection beams could not be π-polarized, so they were left unpolarized.

The injection beams and the collection line of sight were focused to intersect at a fixed point with diameter $\sim$ 1.5 mm, and the thruster was translated on a two-axis motion stage assembly in order to interrogate different regions of the plasma. Alignment with low-power visible lasers and the infrared (IR) laser was carried out using during hardware setup and also each day prior to commencing data collection, after warming up the thruster for at least 1.5–2 hours. The injection optics were mounted on remotely controlled fine motion stages, enabling in situ alignment adjustments under vacuum. The thruster motion stage positions were monitored with inductive linear encoders, and the overall uncertainty in the position of the measurement volume with respect to the thruster was estimated to be $\sim$ 0.5 mm.

The IR laser power into a 1.5 mm diameter spot at the interrogation location was measured to be 27 mW for the axial injection beam, 32 mW for the East injection beam, and 68 mW for the West injection beam (the difference between the East and West intensities arose from an unequal beam splitter on the optical table, and the axial beam intensity was reduced by the polarizer used in this injection optic). These intensities implied that the LIF transition was moderately saturated.[12] Based on a study carried out during another LIF campaign with a similar setup,[35] it appears that saturation could have caused the mean ion velocity along each direction to be underestimated by up to 500 m/s. However, comparisons between axial velocities obtained from direct axial injection versus a linear combination of the East and West direction velocities, along with results from LIF measurements using lower laser intensity on HERMeS TDU-1 at GRC,[13] implied that the distortion was negligible for the axial direction.

III. Time-Averaged LIF

A. Random Uncertainty in the Mean Velocity

Previous studies[4, 14, 15] have found that the ions that cause pole erosion in magnetically shielded thrusters probably originate primarily from the edges of the beam. Knowing the shape of the potential contours in these regions is therefore critical for making accurate erosion predictions, and a major focus of the second HERMeS TDU-2 LIF campaign was to extend the previous datasets[8, 13] to cover more area in the beam edges, with greater spatial resolution. Due to the low plasma density in these regions, many of the IVDFs had low signal-to-noise ratio (SNR). In order to facilitate validation of the hydrodynamic simulations, it was important to quantify the uncertainty in the mean velocities calculated from the first moment of the IVDFs.

LIF studies on Hall thrusters often produce noisy data, but it is not common in the community to see error bars on velocity plots. In space physics, Monte Carlo resampling techniques have been successfully applied to estimate uncertainties in moments of velocity distributions measured by particle detectors.[37] We have adopted the resampling technique known as bootstrapping[38, 39] for the analysis of laboratory LIF data. The basic principle is to randomly sample from the measured dataset (LIF signal as a function of laser wavelength or equivalently ion velocity) with replacement (i.e., a single measured data point can be included in the set more than once) in order to create a new bootstrap dataset, which contains the same number of points as the original dataset but usually does not include every measured data point. A large number ($\sim$ 10000) of bootstrap datasets are generated, and the first moment, $\langle v\rangle = \left(\int v f(v)\, dv\right) / \left(\int f(v)\, dv\right)$ (where $f(v)$ is the IVDF), is calculated for each one. The variance in the bootstrap mean velocities approximates the variance that would be expected had the LIF IVDF been measured many times, instead of just once.

Some examples of bootstrap datasets generated from a single measured IVDF are shown in Fig. 2. After calculating the standard deviation σ of $\langle v\rangle$ for the ensemble of bootstrap datasets, we apply error bars spanning $\pm 2\sigma$ around the measure mean velocity. The implication is that if ion velocities predicted by Hall2De simulations fall outside of these error bars, we can conclude with 95% confidence that the model is not calculating the correct velocity. This statement is not strictly true because the error bars include only random uncertainty in the mean velocity, while systematic uncertainty also exists. In addition to the possible saturation effect discussed in Sec. B, the accuracy of the wavelength meter used in this study corresponded to velocity uncertainty of $\pm$50 m/s, and knowing the target atomic transition wavelength to only three decimal places (834.953 nm) implies a velocity uncertainty of $\pm$180 m/s (no stationary wavelength reference was used). Nevertheless, bootstrapping proved to be a valuable tool for uncertainty quantification, particularly when the data was noisy enough that the random uncertainty dominated.

After calculating the uncertainty in the mean velocity along each laser injection direction, the uncertainty in the direction α and magnitude $|v|$ of the velocity vector could be calculated from standard error propagation

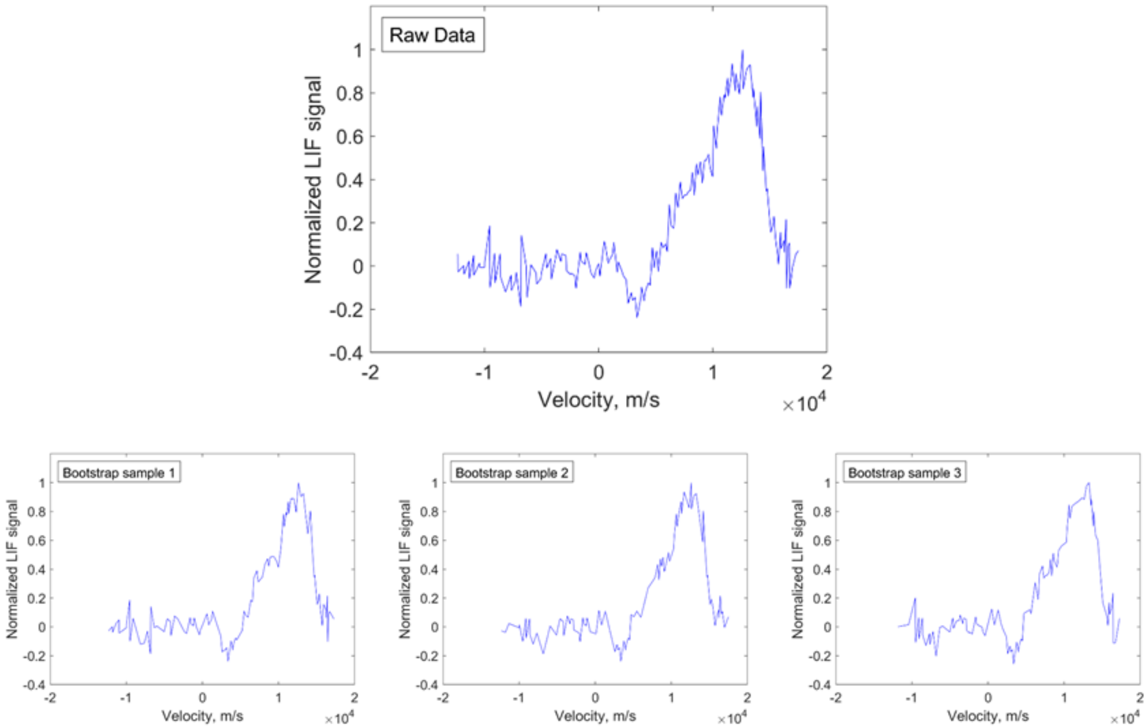

Figure 2. Examples of resampled LIF datasets for an analysis of the mean velocity uncertainty using bootstrapping.

methods. For example, with velocity components measured along the "East" and "West" directions shown in Fig. 1, the standard deviation in the angle was:

$$\sigma_\alpha \approx \sqrt{\left(\frac{\partial \alpha}{\partial v_{East}}\right)^2 \sigma^2_{v_{East}} + \left(\frac{\partial \alpha}{\partial v_{West}}\right)^2 \sigma^2_{v_{West}}}. \tag{1}$$

Note that this expression is derived from a Taylor expansion and thus it becomes inaccurate when σ_{East} and/or σ_{West} are large. In Secs. III.B and III.C, we will give examples of two possible ways to illustrate the uncertainty in the velocity vector, showing either the angle uncertainty only or the overall uncertainty in the location of the vector tip.

B. Beam Measurements

Along the HERMeS throttle curve at fixed discharge current $I_d = 20.83$ A,[40] the global discharge oscillation behavior undergoes a dramatic transition between $V_d = 400$–500 V. At the lower discharge voltages, the discharge current oscillations are low-amplitude and aperiodic, while at the higher voltages, the oscillations are quasi-periodic and have high amplitude.[8] When accounting for these oscillations, including assumed axial movement of the acceleration region inferred from time-averaged LIF data,[8] Hall2De simulations[4] have been able to accurately reproduce the measured pole erosion rates at high V_d.[19,20] However, no satisfactory explanation has been found for the higher-than-expected pole erosion rates measured at lower V_d, particularly 300 V. Since the thruster behavior at 400 and 500 V is similar to that at 300 V and 600 V, respectively, modeling and LIF work has primarily focused on understanding the bounding cases at 300 and 600 V.

Earlier studies[4,8,13] found some disagreement between measured and simulated ion velocity vectors in the beam edges at 300 V. Therefore, a modeling effort was undertaken in which LIF data[13] at the beam edges were used to directly determine the plasma potential contours in the simulation, rather than calculating them self-consistently. The inner pole erosion rates in these simulations[11] were still well below the measured rates. However, the spatial resolution and SNRs of the previous datasets left some ambiguity about the details of the potential contours in the crucial beam edge regions near the channel exit.[11] Therefore, we

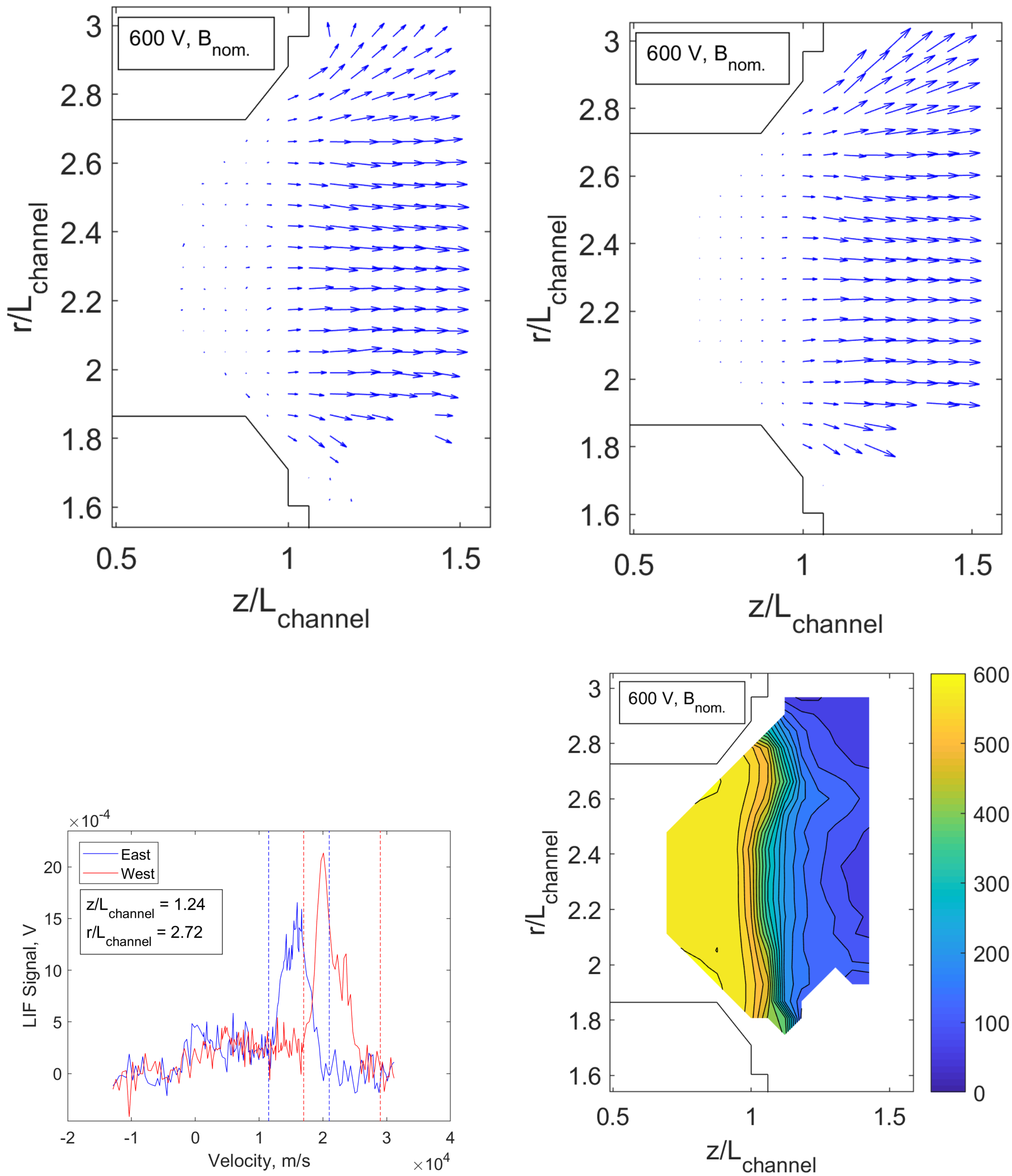

Figure 3. Time-averaged LIF results in the channel and near plume at $V_d = 600$ V, $I_d = 20.83$ A, and $B = B_{nom.}$. Upper Left: Mean velocity vectors obtained by integrating over the entire IVDF. Upper Right: Mean velocity vectors obtained by integrating over only the "fast" ion population born near the anode potential. Lower Left: Example of IVDF data at one location, with dashed lines showing the integration bounds used for the "fast population" mean velocity calculation. Lower Right: Plasma potential contours estimated from the fast population kinetic energies.

carried out additional measurements with the spatial density of points doubled, and the optics arrangement designed to obtain SNR as high as possible.

1. *Results at 600 V*

The dataset at 600 V, 20.83 A spanned the entire width of the channel and the beam edges, enabling comprehensive validation of the simulated velocity vectors at this condition. The results are shown in Fig. 3. Here and throughout the paper, distances are normalized to the thruster channel length $L_{channel}$. The upper left panel shows the mean velocity vectors obtained by integrating over the entire measured IVDF. Data points with unacceptably low SNR were omitted from the plot. Most of these points were in the inner beam edge, which is expected given that there was more bright, dense plasma between the collection optic and this measurement location than there was when probing at larger radii (also, apparently, the metastable target population was low here).

Some of the IVDFs (mostly far from the channel centerline) contained a measurable population of ions created from charge exchange and ionization within and downstream of the acceleration zone; in order to estimate the plasma potential from the data, it was desirable to exclude these “slow” ions from the first moment integral. A vector plot for only the “fast” ions born near the anode potential is shown in the upper right panel of Fig. 3. The lower left panel shows an example of the integration range used for the calculation. The lower bound was somewhat subjective, and some error was introduced by imprecise accounting for the true shape of the fast population’s velocity distribution in the region where it overlapped with the slow population. Nevertheless, this technique has proven to be a valuable tool for comparisons with simulations, giving smoother plots of velocity versus position than those obtained from curve fits or using only the most probable ion velocity. For the HERMeS $V_d = 600$ V dataset in particular, it was important not to confuse two-peaked IVDFs caused by acceleration zone movement[8] with those consisting of two distinct ion populations—this possible ambiguity did not exist at $V_d = 300$ V, nor in other thrusters with negligible acceleration zone movement.[35]

The lower right panel of Fig. 3 shows the plasma potential contours obtained by assuming ions traveling at the mean “fast” population velocity were born at the anode potential and applying conservation of energy. A similar calculation was performed in previous experimental and modeling work.[8,11] This contour map has sufficient spatial resolution for precise comparisons with the Hall2De-calculated potential, although the SNR in the inner beam edge and very near the chamfers was too poor to obtain useful information about the potential in these regions. Note that due to the nonlinear relationship between ion velocity and potential, the potentials calculated from the time average of oscillatory mean velocities may differ slightly from the actual time-averaged potential.

2. *Results at 300 V*

At $V_d = 300$ V, LIF data from previous campaigns were sufficient to validate the simulated ion velocity vectors near the center of the channel, but more information was needed in the beam edges. In addition to addressing the overall discrepancy between simulated and measured inner pole erosion rates, there was interest in the scaling of erosion with magnetic field strength. Simulations have predicted higher erosion at lower magnetic field settings at 300 V,[4] consistent with the expectation that the more downstream location of the acceleration region at low B exposes the poles to more high-energy beam ions.[8,15] However, the opposite erosion trend was measured in recent 200–250 hour wear-test segments on HERMeS TDU-3.[41]

High-resolution LIF data in the beam edges were acquired at $V_d = 300$ V, $I_d = 20.83$ A, and magnetic field strengths of 75%, 100%, and 125% of the nominal field $B_{nom.}$. Figure 4 shows the fast population velocity vectors in the outer and inner beam edges. Data points were omitted if the fast ion population could not be reliably identified, or if the SNR was so poor that no useful velocity information could be obtained.

Both figures show that the beam ion velocity vectors had greater radial divergence at the highest magnetic field strength than at the two lower field settings. This trend, which is not currently reproduced in simulations, seems likely to contribute to the higher pole erosion at $B = 1.25B_{nom.}$. Comparisons in Refs. 12 and 4 previously found that the measured velocity vectors at the 300 V, $B_{nom.}$ condition were more divergent than the simulation predictions (and more divergent than measured vectors at $V_d = 400$ V and 600 V). Explaining the beam divergence trends thus appears to be a key piece of the picture for understanding pole

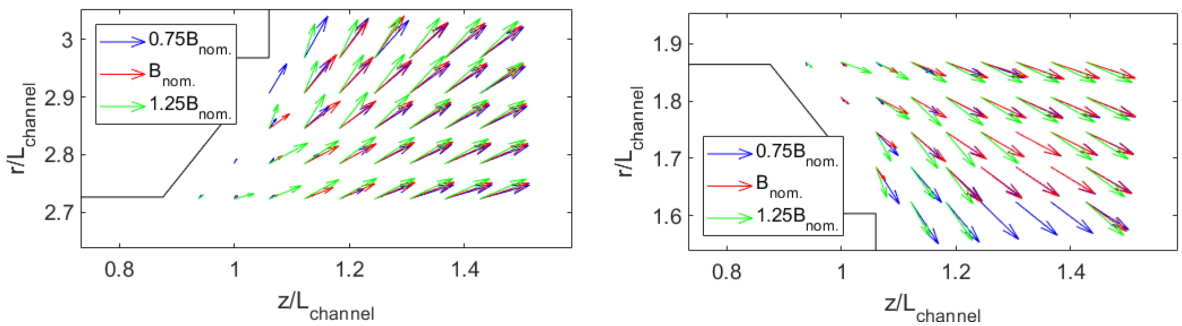

Figure 4. Time-averaged velocity vectors for the fast ion population in the outer (left) and inner (right) beam edges at $\mathbf{V_d = 300}$ V and $\mathbf{I_d = 20.83}$ A, for three different magnetic field strengths.

erosion at 300 V (although the results in Ref. 11 suggest that it is not the only explanation for the existing model/data discrepancy).

The plasma potential is expected to vary along magnetic field lines according to the Boltzmann relation:[11,42]

$$\phi \approx \phi_0 + \frac{k_B T_e}{e} \ln\left(\frac{n_e}{n_{e0}}\right), \tag{2}$$

suggesting that differences between the electric field structure at different magnetic field strength settings (which have approximately the same magnetic topology) must result from differences in electron temperature or in the ratio of the electron density at the beam edges to the channel centerline density. However, modeling studies to date have been challenged to reproduce the measured velocity vectors with reasonable n_e and T_e, suggesting that there may be a mechanism causing deviations from Eq. 2 in the vicinity of the acceleration region.[11]

3. Comparisons Between Measurements at JPL and GRC

Overlaps between the data matrices covered by LIF campaigns at JPL and GRC in 2018 provided an opportunity to assess the consistency/reproducibility of the HERMeS LIF data across different thrusters (TDU-2 versus TDU-1) facilities (JPL's Owens Chamber versus GRC's VF6), LIF hardware arrangements, alignment techniques, and analysis methodology for calculating mean velocities (first moment versus curve fitting). The background gas pressures in the two chambers during thruster operation were within 10% of one another. Figure 5 shows a comparison of the fast population velocity vectors measured at the $V_d = 600$ V, $I_d = 20.83$ A, $B = B_{nom.}$ operating condition. Very close overall agreement between the two sets of vectors is evident. The measured acceleration zone location was slightly further upstream for TDU-2 in Owens chamber (as evidenced by the longer velocity vectors at $z/L_{channel} = 1.06$), but the difference was only on the order of the estimated position uncertainty for the two datasets. Small differences in the vector directions were observed toward the edges of the beam.

A more detailed comparison was carried out for the 300 V operating conditions. Unlike in Fig. 5, for this comparison mean velocities for both datasets were calculated from the first moment of the raw IVDF data in order to enable uncertainty analyses following the bootstrapping methodology described in Sec. III.A In light of the difficulty understanding the pole erosion mechanisms at this discharge voltage, as well as variations of up to a factor of 2 between measured erosion rates across different HERMeS test campaigns and at different times during the same wear test,[19,20,41] there was significant interest in determining whether subtle facility effects or other unknown variables could substantially affect the ion velocities in the beam edges. Velocity vector comparisons for the $V_d = 300$ V, $B = B_{nom.}$ condition are shown in Fig. 6.

In order to more clearly illustrate trends in the vector angles, unit vectors (with no information about the relative velocity magnitudes) are plotted. Uncertainty ranges for the angles were calculated using Eq. 1; the 95% confidence bounds are displayed with dashed arrows on either side of the solid arrow showing the most likely vector direction. Only at locations where the uncertainty ranges for the TDU-2 data (Owens chamber at JPL) and the TDU-1 data (VF6 chamber at GRC) did not overlap can we confidently conclude that the ion velocities in the two thrusters differed. The most notable result was that the TDU-2 velocity vectors had consistently greater radial divergence in the inner beam edge than the TDU-1 vectors, a feature

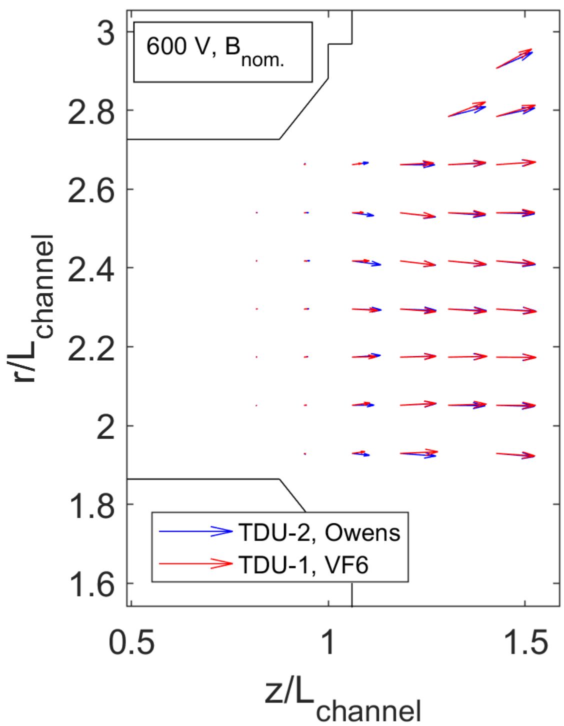

Figure 5. Comparison of time-averaged fast population velocity vectors at the $\mathbf{V_d = 600}$ V, $\mathbf{I_d = 20.83}$ A, $\mathbf{B = B_{nom.}}$ operating condition measured for HERMeS TDU-2 in JPL's Owens Chamber and for HERMeS TDU-1 in GRC's VF6 (these data were originally published in Ref. 13).

that would be expected to affect pole erosion. When first moment integration was carried out over the full IVDF (lower-left panel of Fig. 6), only the differences at $z/L_{channel} < 1.2$ were statistically significant. Limiting the integration range to consider only the fast ion population (lower-right panel) reduced the uncertainty calculated from bootstrapping, and the greater divergence of the TDU-2 vectors was significant at all seven locations studied. In the outer beam edge (top panels of Fig. 6), the opposite trend was noted at $z/L_{channel} = 1.18$, $r/L_{channel} = 2.78$ and 2.91 (the TDU-1 vectors were more divergent than the TDU-2 vectors); however, at the first of these locations the difference was primarily due to a larger slow ion population in the TDU-1 test, while the fast population vectors were nearly identical.

Similar results were obtained at the $V_d = 300$ V, $B = 0.75B_{nom.}$ condition, which was also studied in detail. The variation in beam edge ion velocity vectors between different TDU thrusters and test facilities is consistent with the observed variations in measured pole erosion rates at a given operating condition. The reason for this velocity variation is not understood presently. Given the sensitivity of Hall2De pole erosion predictions to the details of the beam edge potential contours,[4,11,15] this data presents another challenge for modeling the HERMeS 300 V operating conditions.

C. Cathode Plume Measurements

Hall2De simulations of HERMeS include the cathode plume region along the thruster axis, incorporating the interior cathode solution from the stand-alone cathode code OrCa2D[43,44] as a boundary condition. 2D LIF measurements were carried out at $I_d = 20.83$ A and $V_d = 300$ V and 600 V during thruster operation in order to validate the plasma solution in the cathode plume. Another goal was to directly detect ions that could erode surfaces near the cathode, if possible. A high rate of cathode keeper erosion exceeding 100 μm/kHr was observed in one wear test of HERMeS TDU-3.[19] However, this occurred only when the cathode was mounted with the keeper face aligned with the pole cover faces; in other HERMeS tests with the cathode recessed in a slightly more upstream position so that its line of sight to the beam was partially shielded by the pole covers, the erosion rate was much lower, suggesting that beam ions rather than cathode

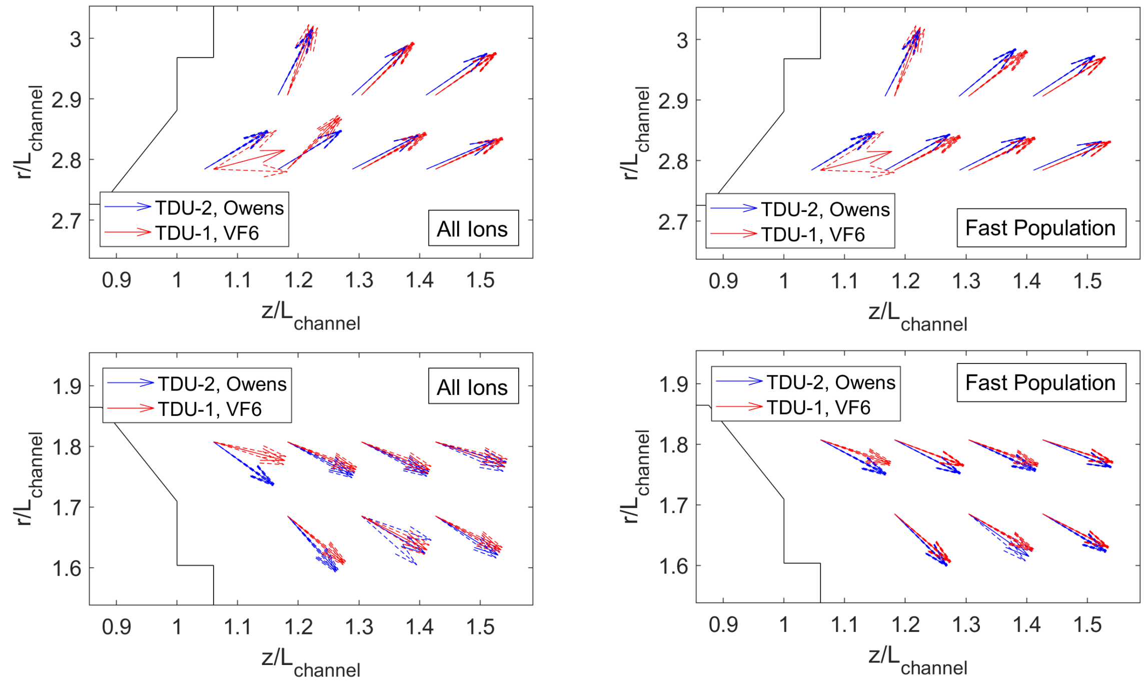

Figure 6. Comparison of time-averaged ion velocity unit vectors at the $\mathbf{V_d = 300}$ V, $\mathbf{I_d = 20.83}$ A, $\mathbf{B = B_{nom.}}$ operating condition measured for HERMeS TDU-2 in JPL's Owens Chamber and for HERMeS TDU-1 in GRC's VF6 (these data were originally published in Ref. 13). 95% confidence bounds for the vector angle, calculated from a bootstrapping analysis of the raw data, are denoted with dashed arrows. Left: Mean velocities including all ions detected in the outer beam edge (top) and inner beam edge (bottom). Right: Mean velocities in the outer beam edge (top) and inner beam edge (bottom) for the fast ion population born near the anode potential.

ions were the primary driver of the erosion. In the recessed cathode configuration, a high erosion rate was observed on the cathode-facing inner edge of the inner pole cover,[20] but this test was carried out with molybdenum pole covers, so it is possible that the energies of the ions causing the erosion were below the sputtering threshold for HERMeS' standard carbon pole covers.

The velocity vectors in the cathode plume measured with LIF are shown in Fig. 7. In addition to the nominal magnetic field cases at V_d = 300 and 600 V, a high magnetic field case at 600 V was studied because this condition had the highest keeper erosion rate when the cathode was in its downstream position (however, note that for the LIF campaign the TDU-2 keeper was in a recessed upstream position). The vectors were calculated from the first moment of the IVDFs along the East and West injection directions (see Fig. 1), with integration bounds chosen to encompass all detectable ion populations. In these figures, uncertainties calculated from bootstrapping (see Sec. III.A) are displayed in an alternate way, with a circle of radius $\sqrt{\sigma^2_{v_{East}} + \sigma^2_{v_{West}}}$ drawn around the vector tip to illustrate the bounds within which the actual vector tip is likely to lie.

The mean ion velocities in the cathode plume were $\lesssim 5$ km/s, directed primarily radially outwards beyond $r/L_{channel} = 0.2$. The upper-left panel of Fig. 7 shows that the velocity vectors were similar for the three operating conditions studied, supporting the notion that differences in the keeper erosion rates between these conditions were caused by ions originating outside the cathode plume. All three operating conditions had $\langle I_d \rangle = 20.83$ A, but the 300 V and 600 V cases had very different I_d oscillation behavior that could in principle have affected the time-averaged IVDFs in the cathode plume.

Previous experiments and modeling[45] have shown that the plasma potential in cathode plumes has a minimum on axis, implying that the positive radial ion velocities must have been produced by some force other than a radially directed electric field. The non-zero v_r values measured at $r = 0$ may have been caused by slight misalignment of the cathode and/or the LIF measurement volume (both of which had uncertainty $\lesssim 1$ mm), or by an asymmetry in the cathode plume itself.

Noting that xenon ions with $v = 5$ km/s have kinetic energy of only ~ 17 eV, ions moving at the mean

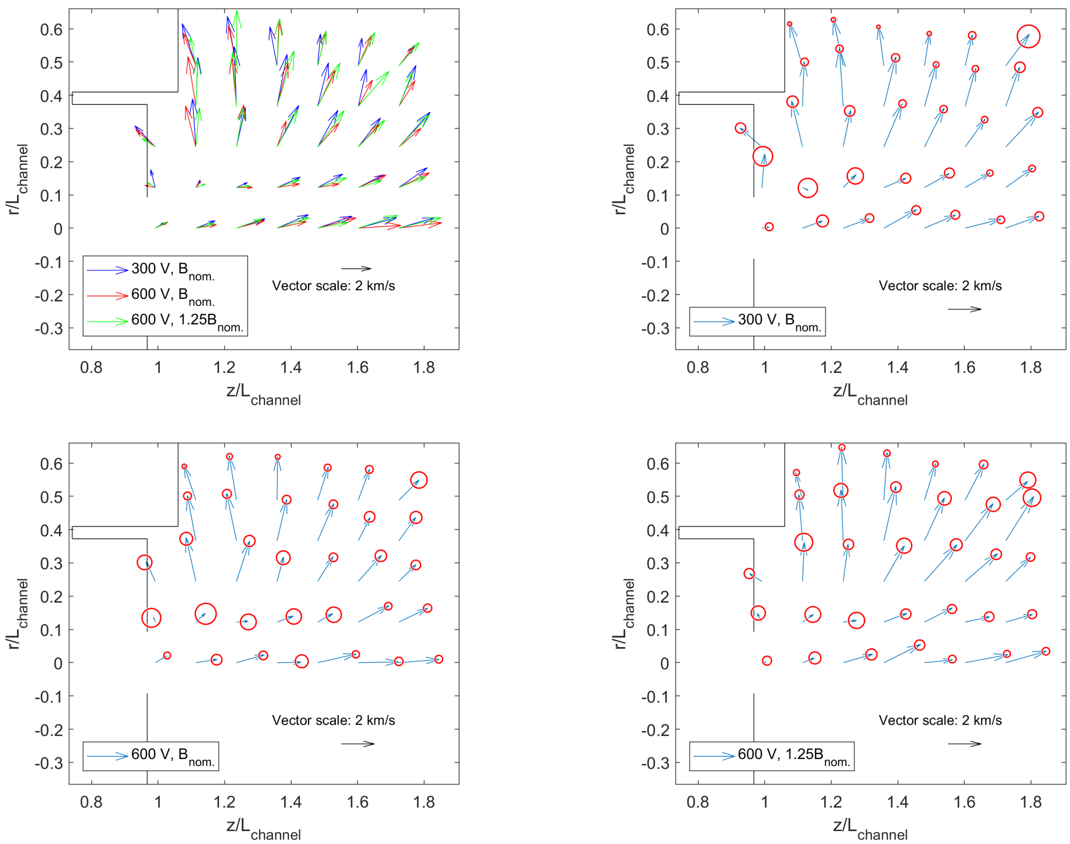

Figure 7. Mean velocity vectors in the cathode plume during HERMeS TDU-2 operation at $\mathbf{I_d = 20.83}$ A. The cathode keeper is centered at $\mathbf{r/L_{channel} = 0}$, and the feature in the upper left corner of each plot is the inner pole cover. Upper left panel: Overlaid vectors from the three operating conditions tested. Upper right and lower left/right panels: Vectors for the three individual conditions, with circles showing the estimated uncertainty range for the location of the vector tip.

velocities shown in Fig. 7 would not have been able to sputter the carbon pole covers and cathode keeper significantly.[46] However, the IVDFs at large radii had a substantial energy spread, which can be quantified using the second moment expression:

$$\Delta E \equiv \frac{M_i \int (v-u)^2 f(v)\, dv}{\int f(v)\, dv}, \tag{3}$$

where $u \equiv \langle v \rangle$ is the mean velocity calculated from the first moment. The energy spread ΔE may be thought of as an effective ion temperature—it is equal to the usual definition of temperature when $f(v)$ is a Maxwellian distribution—but note that the IVDFs with large ΔE were in general non-Maxwellian, non-isotropic, and often appeared to consist of multiple ion populations. With further work it may be possible to make separate vector plots and temperature maps for the different populations, but this was not done for this paper.

The measured energy spreads and examples of IVDFs at locations near and far from the keeper orifice are shown for the $V_d = 300$ V, $B = B_{nom.}$ condition in Fig. 8. Results at the other two operating conditions were qualitatively similar. The energies spreads were < 2 eV on axis near the orifice but reached 10–30 eV at $r/L_{channel} \approx 0.4$, with larger values along the radially outward diagonal direction. Note that no correction to ΔE has been made for Zeeman splitting or other spurious line broadening effects,[14,36] but these should only appreciably affect the narrowest measured IVDFs.

The large ion energy spread implies that cathode ions detected by LIF may make a non-negligible contribution to the erosion of the pole if the flux of these ions striking it is sufficiently high. The plasma density in this region has not yet been measured, however. Also note that front pole erosion has not been seen in

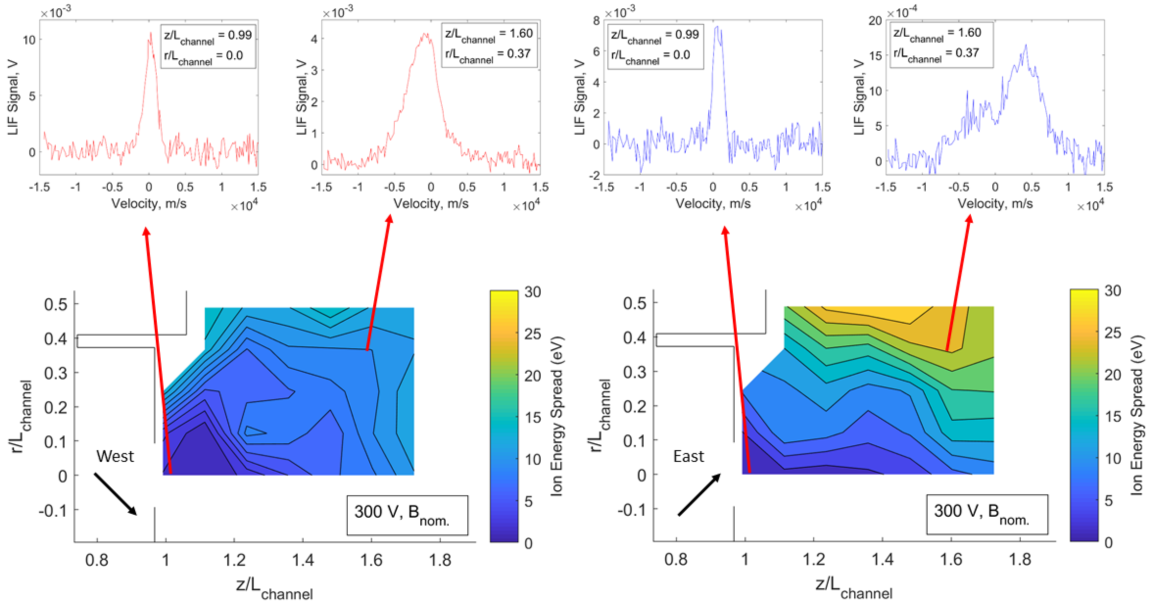

Figure 8. Ion energy spreads in the cathode plume at 300 V, I_d = 20.83 A, and B = $B_{nom.}$, calculated using Eq. 3. The black arrows labeled "East" and "West" in the lower left corner of the contour plots specify the axis along which each IVDF was measured. Examples of narrow and broad IVDFs measured along each direction are shown.

unshielded thrusters with centrally mounted cathodes,[47] and it is not clear why magnetic shielding would affect the cathode plume in a significant way. Similarly broad IVDFs have been detected in front of the inner pole of HERMeS TDU-1[13] and the (magnetically shielded) H6MS thruster.[14] Since measurements of this kind have not been performed in the (unshielded) H6US, it is not known whether such broad distributions exist in this thruster as well. The source(s) of these IVDFs is currently under investigation.

IV. Time-Resolved LIF (TRLIF)

A. Motivation for TRLIF

As noted in Sec. I, HERMeS has two distinct global discharge oscillation regimes (see Fig. 9), with aperiodic, low-amplitude oscillations at V_d = 300–400 V and quasi-periodic, high-amplitude oscillations at V_d = 500–600 V. These large amplitude oscillations are accompanied by the appearance of two peaks in the IVDFs in the acceleration region. Refs. 12 and 8 argued that these bimodal IVDFs were evidence for back-and-forth motion of the acceleration region—when this motion was incorporated in Hall2De simulations by making the position of the anomalous collision frequency profile oscillate in time, measured pole erosion rates at 500–600 V were accurately reproduced.[4] However, direct confirmation of the acceleration zone movement was needed to be confident in the validity of the thruster life models. Furthermore, oscillations in the beam edge potential contours were considered as a possible mechanism to enhance erosion at V_d = 300 V. Therefore, time-resolved LIF (TRLIF) measurements were pursued.

B. TRLIF Method

Transfer Function Averaged LIF[21–23] is the first time-resolved LIF technique developed to be compatible with undriven aperiodic oscillations in electric thrusters, making it applicable to all HERMeS operating conditions. It was originally demonstrated and validated on a hollow cathode with driven oscillations[23] and then through a limited set of measurements on the H6 thruster during operation at $\sim$ 1.5 kW in periodic and aperiodic oscillatory regimes with fundamental I_d oscillation frequency $\leq$ 10 kHz. Application of the technique to HERMeS required extending it to a fundamental frequency exceeding 50 kHz (see Fig. 9), with higher power operation up to 12.5 kW leading to more severe thermal drifts. It was also desired to obtain high SNR while streamlining the data collection and analysis processes as much as possible in order to enable

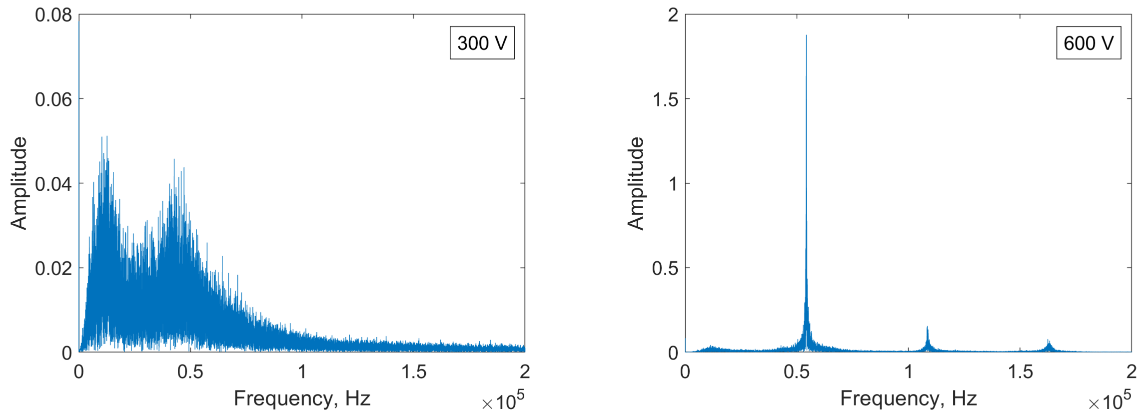

Figure 9. Fourier spectra for discharge current oscillations (measured on the anode line) in HERMeS TDU-2 at $\mathbf{I_d} = \mathbf{20.83}$ A and $\mathbf{B} = \mathbf{B_{nom.}}$. Reproduced from Ref. 12.

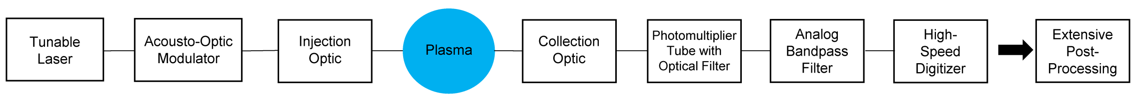

Figure 10. Block diagram of the TRLIF setup.

measurements at a number of spatial locations and operating conditions.

Time-averaged LIF typically uses a lock-in amplifier with a long integration time (≥ 100 ms) to extract the LIF signal from the noise, which is dominated by background light emission. Integrating over a timescale $\ll 20$ μs in order to resolve 50–60 kHz oscillations would not produce sufficient SNR. For undriven, chaotic oscillations, averaging over many oscillation periods is also not an option, so some other averaging procedure is needed. The transfer function averaging approach assumes that a complex-valued function $H(\omega)$ exists that relates the Fourier transform $\hat{l}(\omega)$ of the LIF signal (at a single spatial location and laser wavelength) to the Fourier transform $\hat{r}(\omega)$ of some reference signal:

$$\hat{l}(\omega) = H(\omega)\,\hat{r}(\omega)\,. \tag{4}$$

For studies of global discharge oscillations, the anode current waveform $I_d(t)$ is the most obvious choice for a reference signal, but other choices such as the cathode-to-ground voltage $V_{cg}(t)$ or a local probe signal are also possible. Note that both amplitude and phase information are captured in Eq. 4. The transfer function $H(\omega)$ is assumed to be time invariant at a given thruster operating condition; this does not imply any restriction on the repeatability of the oscillations, but rather says that when a given Fourier component is present in the reference signal spectrum, a component at the same frequency will be present in the LIF signal, and the complex constant of proportionality between them does not vary in time. There is no guarantee that Eq. 4 can completely reproduce the time-variation of the LIF signal; for instance, if the local LIF signal is influenced by an azimuthal mode such as a rotating spoke[48] that does not affect the discharge current waveform, this information will be missing from the reconstructed LIF signal $\hat{l}(\omega)$ calculated from the transfer function using $\hat{r}(\omega) \rightarrow \hat{I}_d(\omega)$. However, the technique is highly effective for breathing mode-like oscillations,[22] and should also be applicable to other types of oscillations at frequency $\lesssim 100$ kHz with an appropriate choice of reference waveform.

A block diagram for the setup used for HERMeS TRLIF measurements is shown in Fig. 10. The acousto-optic modulator (AOM) enabled laser modulation at up to ~ 2 MHz. The fluorescence emission was fiber coupled to a filtered photomultiplier tube (PMT) tube, and the output across a 1 kΩ resistor was passed through an analog bandpass filter and then digitized directly, with no up-front lock-in amplification. Phase sensitive detection (the function of a lock-in amplifier) was performed in post-processing, enabling the data analysis to be repeated multiple times and optimized without losing information.

Phase sensitive detection involves digitally multiplying the data by a sine wave at the laser modulation frequency, creating components near DC (the desired signal) and at twice the modulation frequency. A

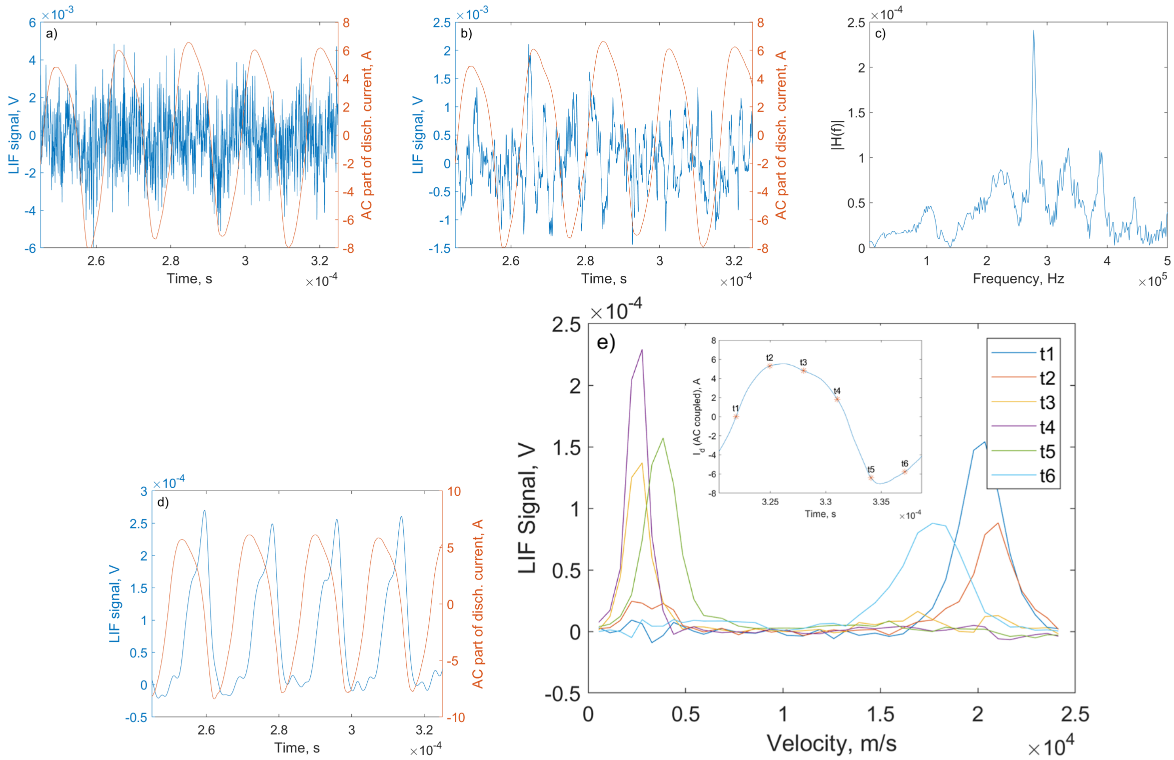

Figure 11. Steps in TRLIF data analysis, illustrated for the laser wavelength corresponding to $v_z \approx 2.7$ km/s at the 600 V, 20.83 A, $B_{nom.}$ operating condition at $z/L_{channel} = 1.01$. a) Raw LIF data following electronic bandpass filtering. b) Demodulated LIF data. c) Transfer function calculated from averaging over all data segments. d) Time domain LIF signal at one wavelength. e) Time-resolved IVDF shown at six times during the discharge current oscillation (the inset specifies the phase of the I_d oscillation corresponding to each IVDF snapshot).

low-pass filter with time constant τ_{PSD} is then applied to exclude the high-frequency component, while also rejecting noise at frequencies far from the modulation frequency. In order to avoid significant distortion of the desired LIF signal, the time constant must be at least ~ 10 times shorter than the desired measurement bandwidth. This requirement is part of a hierarchy of timescales:

$$f_{signal} \ll \frac{1}{\tau_{PSD}} \ll f_{mod} \ll f_{DAQ}, \tag{5}$$

where f_{mod} is the laser modulation frequency and f_{DAQ} is the data sampling frequency. For HERMeS, it was desired to resolve LIF signal dynamics at frequencies up to the second harmonic of $\hat{I}_d(\omega)$ at 600 V, which was at ~ 110 kHz. Therefore, for most measurements the low-pass filter time constant was chosen to be $t_{PSD} = 0.7$ μs (i.e., $1/\tau_{PSD} \approx 1.4$ MHz), the laser was modulated at $f_{mod} = 1.8$ MHz, and data was digitized at $f_{DAQ} = 25$ MHz. The laser modulation frequency was limited by the capabilities of the AOM and the electronic filter (Krohn Hite 3944) used to reduce the data's dynamic range prior to digitization, but also in some cases by the necessity to acquire many signal photons per modulation period. Since τ_{PSD} only encompassed ~ 1.25 modulation periods, the LIF signal was still extremely noisy following demodulation. The remaining SNR improvement was accomplished by applying transfer function averaging to a large dataset spanning ~ 30 s of acquisition time.

These parameters led to severe demands on the data acquisition, storage, and post-processing capabilities, which were met with a Sig-Station S03-BCD-T02-C01 supercomputer with dual Intel Xenon 2.2 GHz 12-Core CPUs, 256 GB RAM, and an integrated GaGe Razor Express CompuScope 12-channel DAQ array with 48 GB onboard memory and max sampling rate of 200 MS/s. The system included ~ 50 TB of storage capacity in a RAID 5 configuration, with an additional backup hard drive bank for long-term data storage. Another key hardware component was a precision clock generator (SRS CG635-03) used to synchronize the laser modulation and DAQ timebases and prevent phase drift over the long data acquisition time.

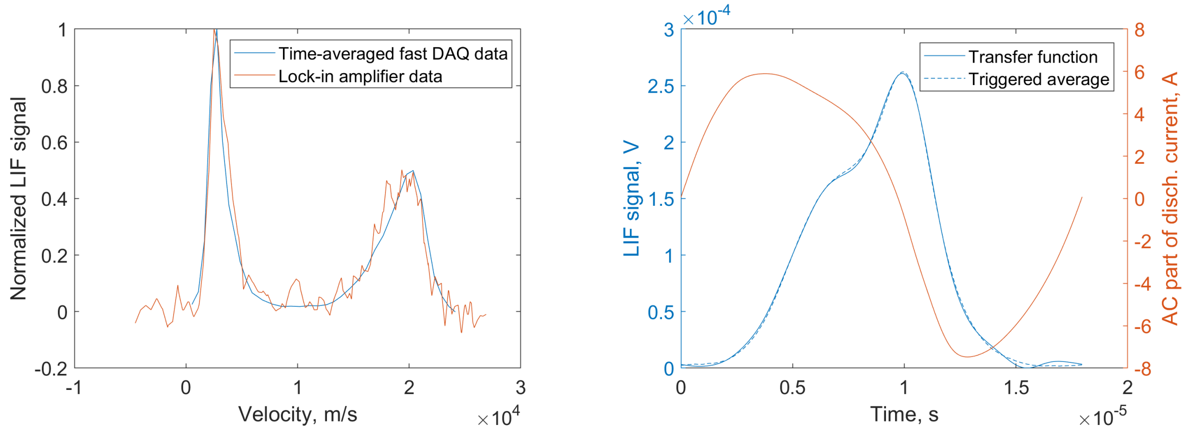

Figure 12. Validation of the TRLIF implementation. Examples are shown for the 600 V, 20.83 A, $B_{nom.}$ operating condition at $z/L_{channel} = 1.01$. Left: Comparison between the time average of the demodulated TRLIF data and a time-averaged IVDF acquired by chopping the laser at 3 kHz and feeding the PMT output to a commercial lock-in amplifier. Right: Comparison of the time-resolved signal at the laser wavelength corresponding to $v_z \approx 2.7$ km/s obtained from transfer functioning averaging versus triggered averaging.

In addition to enabling useable SNRs to be achieved for time-resolved data, transfer function averaging provided a means to synchronize waveforms acquired sequentially at different laser wavelengths, so that the time dependence of the entire IVDF at one or more spatial locations could be calculated. Following Durot's approach,[22] the data was split into ~ 1 ms long segments, and transfer function estimators were calculated for each segment and then averaged together to improve the SNR. The overall data acquisition and processing sequence was as follows (the waveforms after several intermediate steps are illustrated in Fig. 11):

1. At each laser wavelength (~ 40 per spatial location), simultaneously acquire LIF data, discharge current data, and the laser modulation waveform at 25 MHz sample rate for 30 seconds (Fig. 11(a)).
2. Digitally apply phase-sensitive detection with a 0.7 μs time constant in order to isolate the component of the detected signal that is varying at the laser modulation frequency (Fig. 11(b)).
3. Fourier transform ~ 1 ms long segments of simultaneously acquired LIF data and discharge current data and calculate the transfer function estimator for each discrete frequency by solving Eq. 4 for $H(\omega)$.
4. Average the transfer function estimators over thousands of data segments to determine the transfer function with high SNR (Fig. 11(c)).
5. Use a single discharge current signal as the input to the transfer function (i.e., apply Eq. 4) and calculate the Fourier-transformed LIF signal at all wavelengths of interest during a single time interval.
6. Take the inverse Fourier transform to find the time-domain LIF signal at each wavelength (Fig. 11(d)).
7. Combine the signals from all wavelengths to get the time-resolved ion velocity distribution (Fig. 11(e)).

Given the relatively abstract nature of the data analysis, validation of the TRLIF implementation was a critical component of the experimental campaign. Extensive validation of the general method was previously performed by Durot—for details, as well as excellent exposition on the theory and algorithms underlying the technique, refer to Ref. 22. To validate the JPL data acquisition setup and the algorithms for applying phase sensitive detection numerically, the time average of the demodulated data was compared with LIF data acquired using the traditional lock-in amplifier method. An example is shown in the left panel of Fig. 12. In order to accurately map out the IVDF, LIF requires that the ratio of the PMT signal to the number of emitted fluorescence photons remains constant as the laser wavelength is scanned. This condition was not necessarily satisfied for the TRLIF data because the time required to acquire a full IVDF was on the order of 1 hour (compared to $\lesssim 5$ minutes for traditional time-averaged LIF)—long enough for non-negligible thermal drift in the alignment of the injection and collection optics to occur. This issue was partially mitigated by taking time-averaged LIF data at the beginning of each run day before switching over to TRLIF once the system was close to thermal steady state. The remaining distortion of the time-resolved IVDFs was removed by multiplying the data by a wavelength-dependent alignment drift correction factor calculated from a linear fit to the ratio of the lock-in amplifier data amplitude over the time-averaged fast DAQ data amplitude plotted versus wavelength. Assuming that the alignment degradation occurred linearly in time was generally sufficient to produce good validation results comparable to those shown in Fig. 12.

Since the discharge current oscillations were nearly periodic at $V_d = 600$ V, it was possible to validate the transfer function averaging technique by comparing the calculated LIF signal time-dependence with that obtained from a simpler "triggered averaging" analysis[23] in which the rising edge zero crossing of $I_d(t)$ was used as a phase reference to enable direct averaging of the demodulated LIF signal over many oscillation periods. The discharge current waveform was itself averaged over the same number of periods, and the Fourier transform of this averaged $I_d(t)$ was used as the input to the transfer function ($\hat{r}(\omega)$ in Eq. 4) for comparison. An example of the results for a single laser wavelength is shown in the right panel of Fig. 12, with very close agreement evident between the two analysis methods.

C. TRLIF Results

1. *Channel Centerline Measurements*

Time-resolved measurements of axial ion velocities along the channel centerline were carried out at four HERMeS "Reference Firing Conditions" ($V_d = 300, 400, 500, 600$ V; $I_d = 20.83$ A, $B = B_{nom.}$), at five axial locations per operating condition. While the long data acquisition times precluded construction of highly detailed spatial maps as in Sec. III, the selected locations were sufficient to probe the ionization, acceleration, and near plume region dynamics. The results are shown in Figs. 13–16. To produce each set of plots, the transfer function at each spatial location for each laser wavelength was determined from simultaneously digitized LIF data and $I_d(t)$ data, then a single $I_d(t)$ waveform (shown as an inset on the mean velocity plot in the lower right of each figure) was used as the input to the transfer function for all wavelengths and locations in order to synchronize the time-dependent IVDFs and the mean velocities derived from them. IVDFs and mean velocity profiles were plotted at six phases of the I_d oscillation. The electronic bandpass filter and the digital low-pass filter each introduced a phase delay[22] of 0.5–1 μs, which were accounted for when synchronizing the plots. If the assumption that the transfer function is invariant at a given thruster operating condition is valid, then once $H(\omega)$ is known any $I_d(t)$ waveform can be used to reconstruct what the LIF signal at each wavelength and position would have been during a particular time interval, whether or not LIF data was actually acquired.

Referring first to the $V_d = 600$ V data in Fig. 13, the mean ion velocity was nearly stationary at the furthest upstream location ($z/L_{channel} = 0.82$), but the LIF signal amplitude waxed and waned with the discharge current oscillation, peaking near the positive-going zero crossing of $I_d(t)$. Watching an animation of the IVDF gives the impression of "breathing" behavior for which the classic global Hall thruster oscillations are named. However, the discharge oscillations in HERMeS at 500–600 V are at a hgher frequency than would be expected in such a large thruster if the frequency scaled with the neutral transit time across the ionization region,[49] and they may be driven by physics distinct from the breathing mode.

The mean velocity in the acceleration region ($z/L_{channel} = 0.96$–1.06) oscillated between low and high values, confirming the acceleration zone movement that was originally hypothesized based on time-averaged LIF data.[8,12] However, the time dependence was impulsive rather than sinusoidal, with a very rapid transition between the upstream and downstream locations of the region with a high electric field. The acceleration region was furthest upstream near the time of the positive-going zero crossing of $I_d(t)$ and furthest downstream near the negative-going zero crossing. The mean velocity $u_z(t)$ at $z/L_{channel} = 1.01$ is plotted in the left panel of Fig. 17, illustrating the steep transitions from low to high velocity and back. Interestingly, Hall2De simulations that were carried out prior to the TRLIF study with an imposed sinusoidal oscillation of the anomalous collision frequency profile also produced a $u_z(t)$ oscillation that was closer to a square wave than a sinusoid, as shown in the right panel of Fig. 17. Other than the vertical offset between the two plots, which was due to a small difference in the mean acceleration region location in this simulation compared to the latest dataset, the model result and measurement were very similar. Thus it was concluded that no adjustments in the simulation parameters were needed based on the new detailed information about the time dependence of the ion velocities.

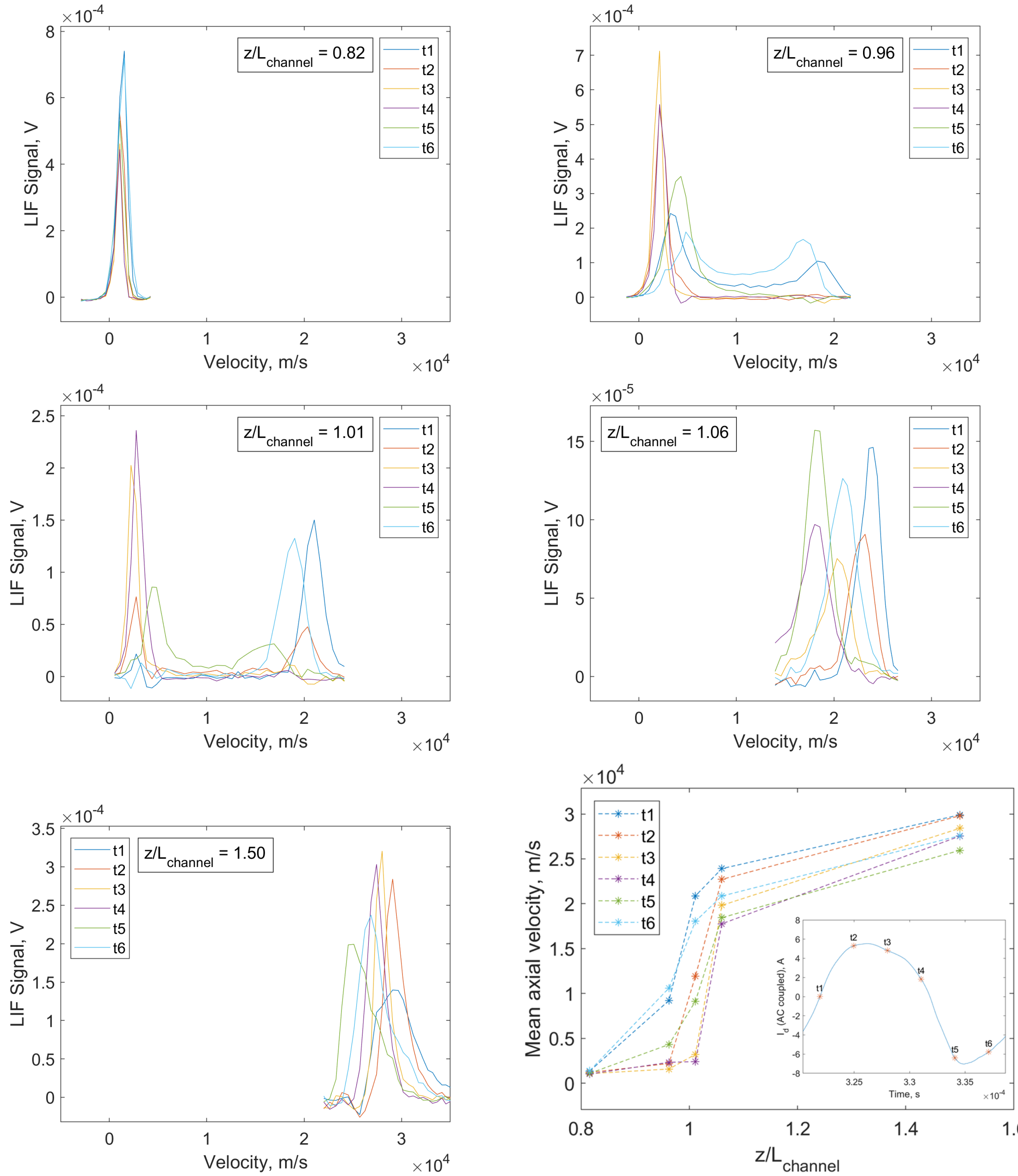

Figure 13. TRLIF results along the channel centerline at $\mathbf{V_d = 600}$ V, $\mathbf{I_d = 20.83}$ A, and $\mathbf{B = B_{nom.}}$. Axial IVDF snapshots are shown at six times during a single I_d oscillation period. The lower right plot shows the mean velocity calculated from the first moment of the time-resolved IVDFs, and the inset shows the discharge current waveform with the snapshot times labeled.

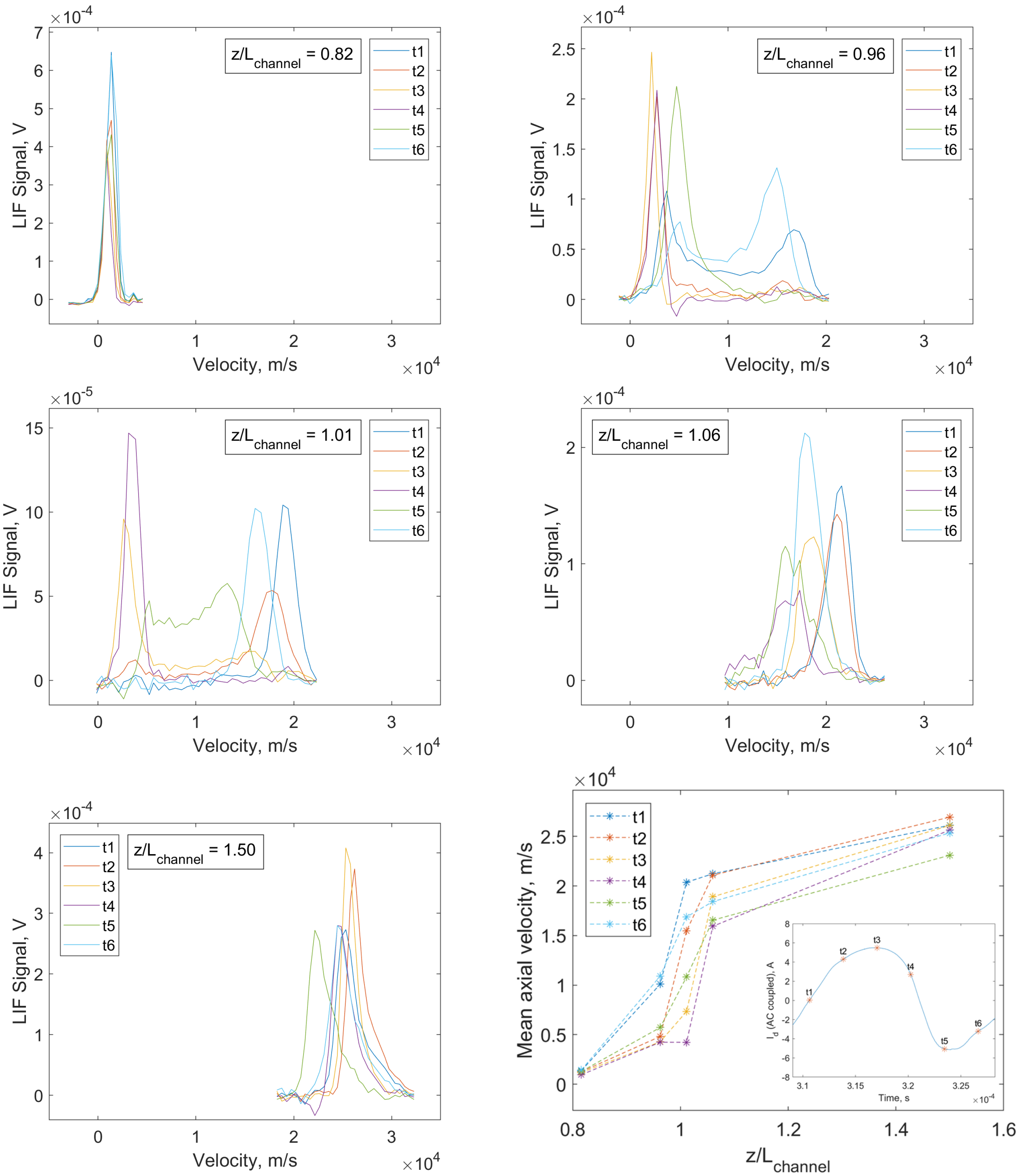

Figure 14. Same as Fig. 13, for $\mathbf{V_d = 500}$ V.

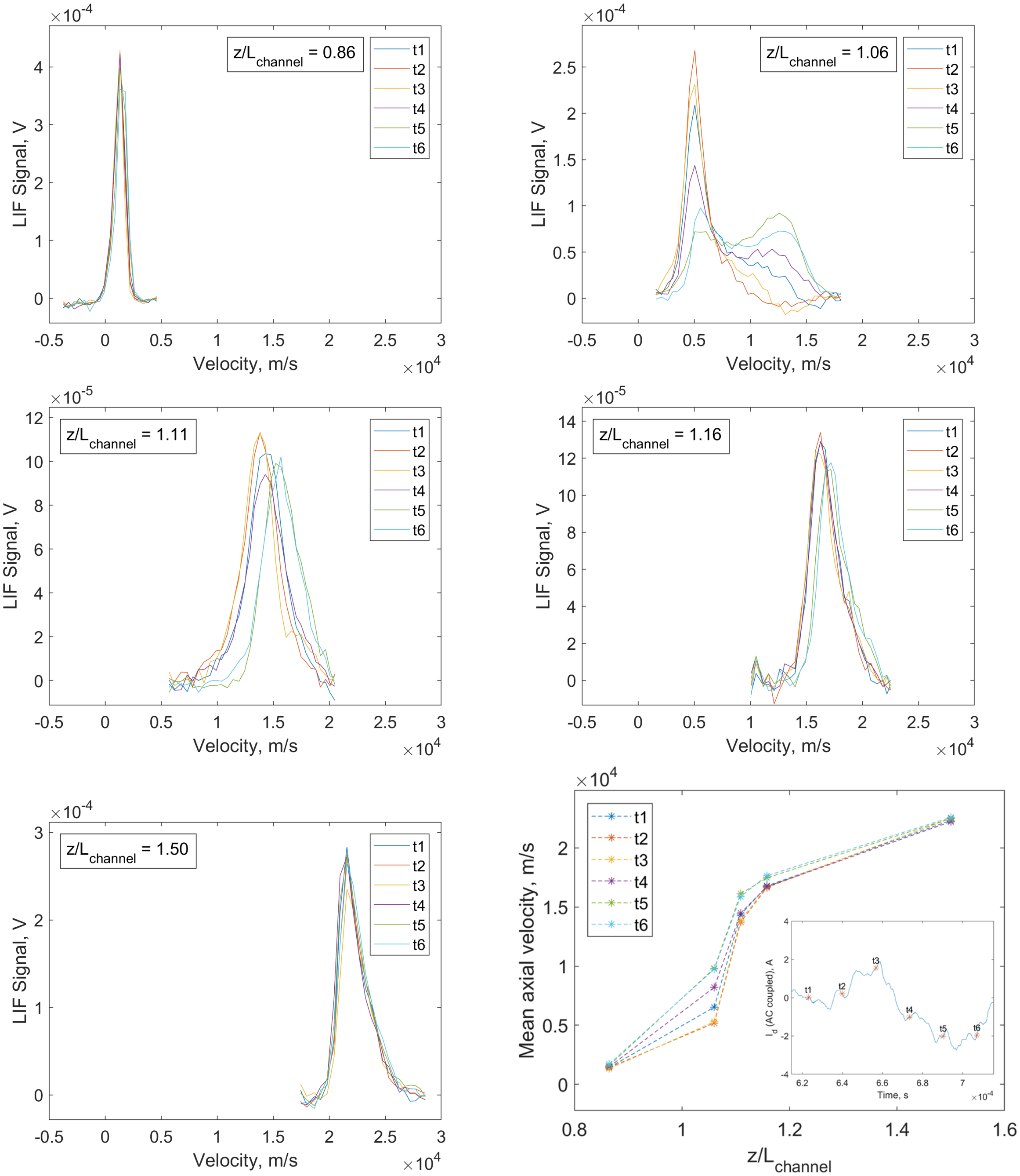

Figure 15. Same as Fig. 13, for $\mathbf{V_d = 400}$ V. $\mathbf{I_d(t)}$ was far from periodic at this operating condition, so the time-dependent behavior displayed is unique to the specific time interval plotted.

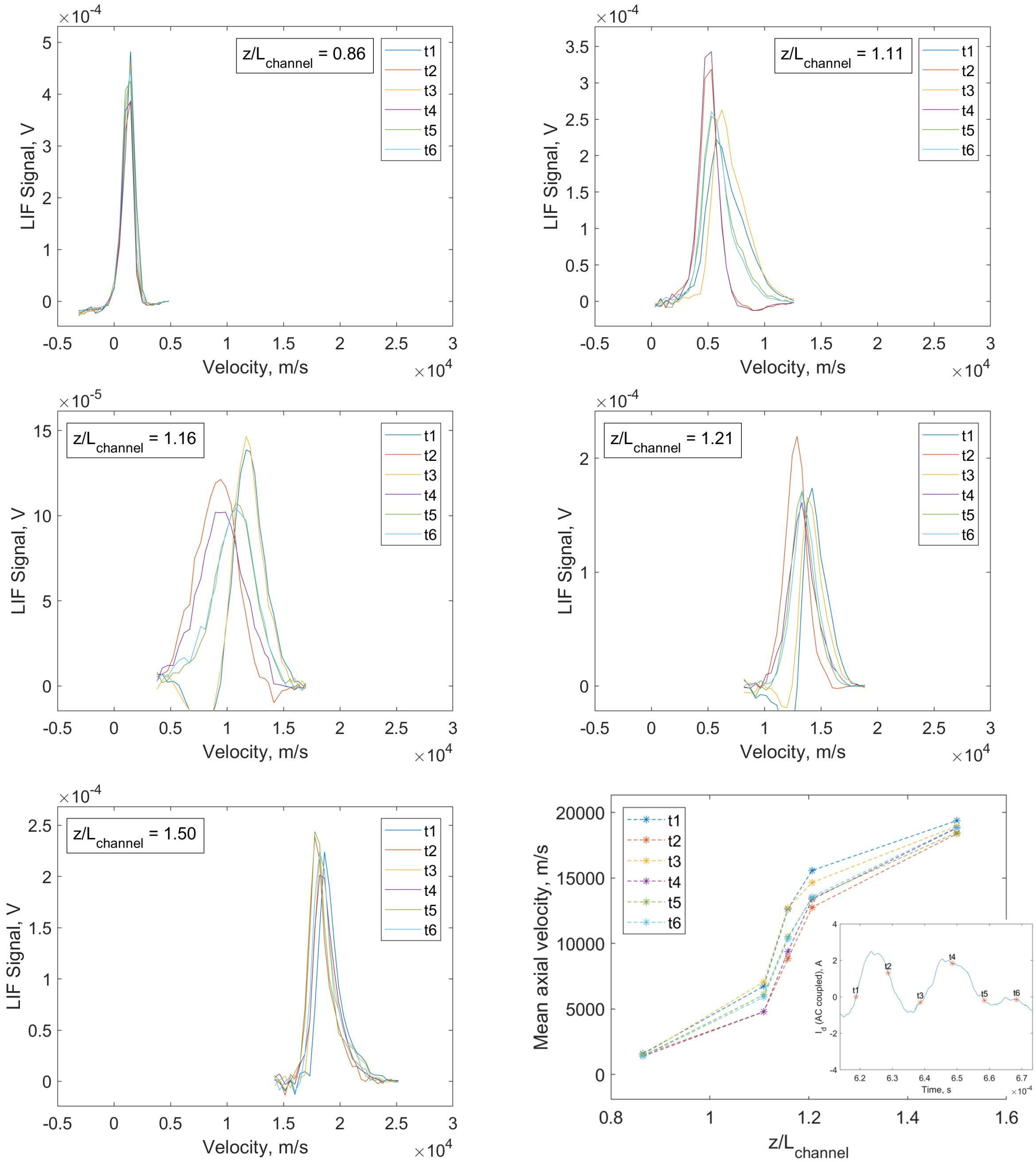

Figure 16. Same as Fig. 13, for $\mathbf{V_d = 300}$ V. $\mathbf{I_d(t)}$ was far from periodic at this operating condition, so the time-dependent behavior displayed is unique to the specific time interval plotted.

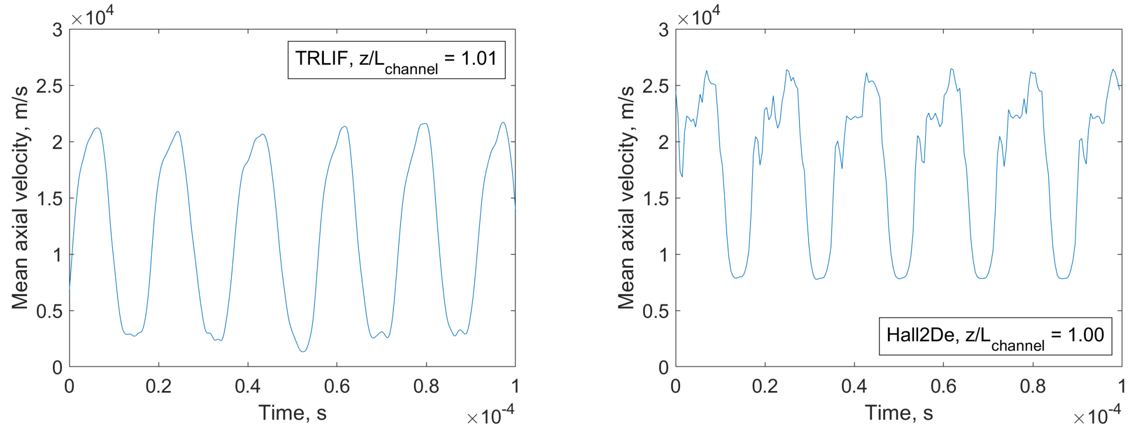

Figure 17. Left: Measured mean axial ion velocity versus time at $z/L_{channel} = 1.01$ at $V_d = 600$ V, $I_d = 20.83$ A, and $B = B_{nom.}$. Right: Mean velocity calculated by Hall2De at the same condition.

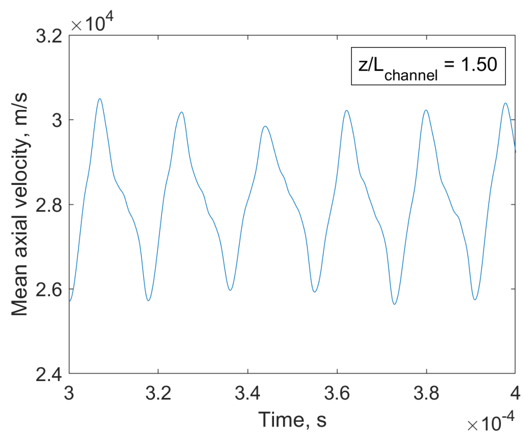

Figure 18. Mean axial ion velocity versus time for the furthest downstream point studied at $V_d = 600$ V, $I_d = 20.83$ A, and $B = B_{nom.}$.

At some instances the IVDFs shown in Figs. 13 and 14 appeared to have simultaneous slow and fast velocity peaks. This was likely an artifact of the finite measurement bandwidth of $\sim$ 100 kHz set by the analog bandpass filter and the digital low-pass filter: during portions of the cycle when the LIF signal at a given laser wavelength was changing much faster than the fundamental oscillation frequency, the diagnostic could not keep up. Similarly, the actual du_z/dt during the transitions may have been even faster than what is shown in the left panel of Fig. 17.

The 500–600 V operating conditions featured an unexpectedly large oscillation in the mean ion velocity in the near plume, as shown in Fig. 18 and also the lower-right panels of Figs. 13 and 14. For the 600 V case, the mean ion velocity at the peak of the oscillation was $\sim$ 30.2 km/s, corresponding to a kinetic energy of $\sim$ 625 eV. The mean velocity at the trough was $\sim$ 25.8 km/s, corresponding to an energy of $\sim$ 455 eV. Part of this energy spread could have been a result of the discharge voltage ripple, which was $\sim$ 70 V peak-to-peak at this operating condition, but the remainder must have been produced by a $\gtrsim$ 100 V peak-to-peak oscillation in the plume potential. Note that the $u_z(z)$ profile was nearly flat at this location,[8] which is not obvious from the mean velocity plots in Figs. 13 and 14 since there are no data points shown between $z/L_{channel} = 1.06$ and $z/L_{channel} = 1.50$, so the contribution of acceleration zone movement to the local mean velocity oscillation was small. Since these oscillations had the same fundamental frequency as the discharge current oscillation, the likely implication is that the $\sim$ 50 kHz global oscillation at the higher HERMeS discharge voltages involves substantial variations in the efficiency of cathode coupling with the plume.

Figures 15 and 16 illustrate the first time-resolved IVDF measurements during non-periodic oscillations

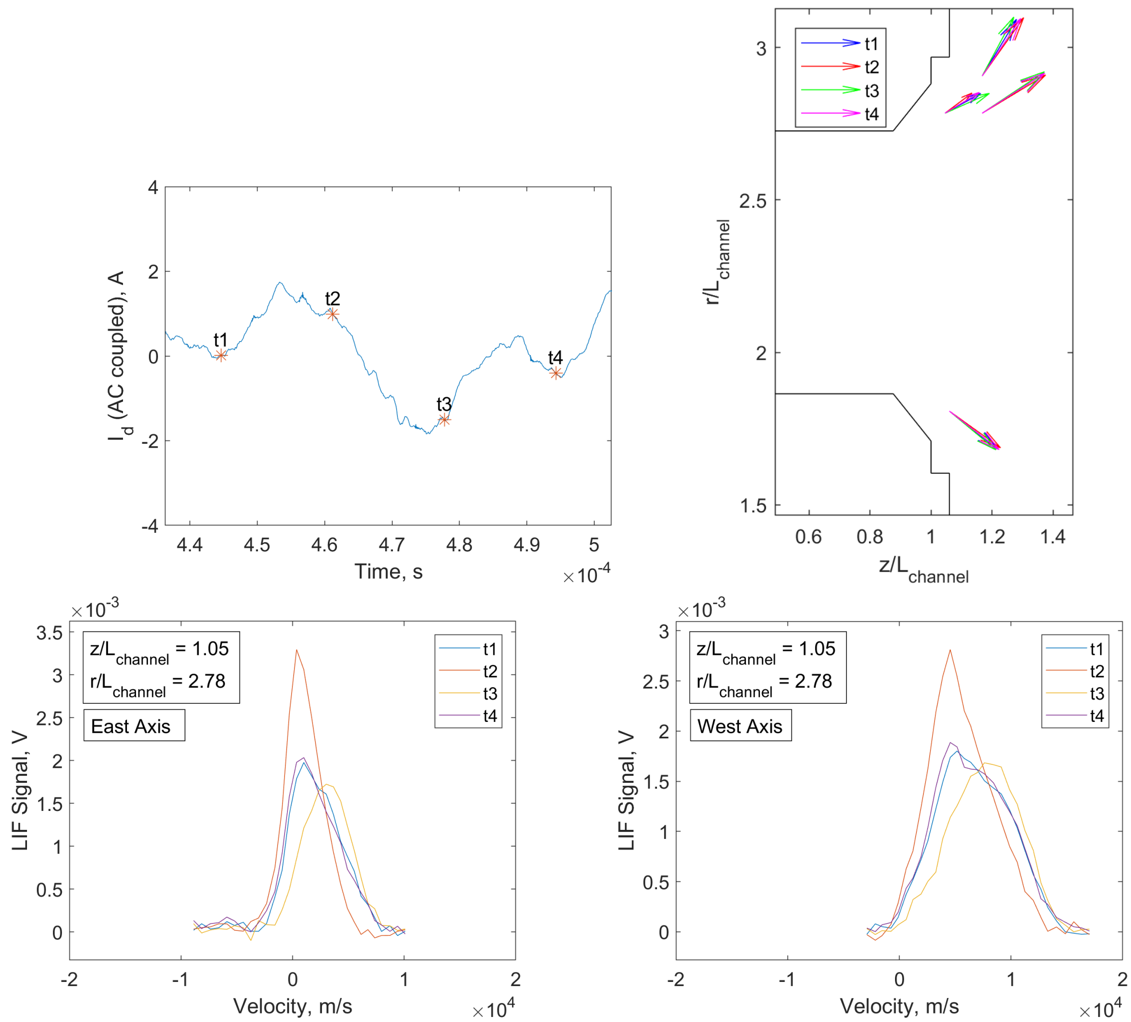

Figure 19. Results from 2D TRLIF measurements in the beam edges at $\mathbf{V_d = 300}$ V, $\mathbf{I_d = 20.83}$ A, and $\mathbf{B = B_{nom.}}$. Upper Left: Discharge current waveform showing times at which IVDF and velocity vector snapshots were plotted. Upper Right: Velocity vectors at the four times. Lower Left and Right: IVDFs along the two measurement direction at the four times ("West" refers to the radially outward diagonal axis—see Fig. 1).

in HERMeS. The dynamic variations were less pronouced than at higher V_d, as expected based on the lower amplitude of $I_d(t)$ oscillations at these operating conditions, but there was still non-negligible movement of the acceleration region that broadened the time-averaged IVDFs at $z/L_{channel}$ = 1.06–1.21. The negative LIF signals in a few of the 300 V plots are indicative of spurious high-frequency content in the transfer function, which might improve with an even larger data sample or different analysis parameters.

Particularly interesting behavior was observed at V_d = 400 V at $z/L_{channel}$ = 1.06. Here the IVDF developed a broadened, roughly bi-modal structure that persisted for 20–40 μs—too long to attribute it to a measurement bandwidth limitation. The time average of the demodulated TRLIF data was good agreement with the time-averaged IVDF measured with a lock-in amplifier (comparable to the result shown in Fig. 12). It is also notable that the near plume potential was essentially constant at V_d = 400 V but varied measurably at 300 V.

2. Beam Edge Measurements at 300 V

Time-resolved 2D velocity measurements were carried out at six positions in the beam edges at the $V_d = 300$ V, $I_d = 20.83$ A, $B = B_{nom.}$ operating condition, seeking to identify dynamics that might help explain the high inner pole erosion rate observed at this condition. The measurement locations were chosen based on proximity to the chamfer and pole corner regions where ions causing the majority of the pole erosion are suspected to originate,[14] reasonably high signal strength and SNR in time-averaged LIF data, and the presence of interesting features such as multiple peaks in the time-averaged IVDFs. Ultimately only four of the locations had sufficient SNR in the TRLIF data to produce useful movies of the velocity vector evolution. Unlike time-averaged LIF, the TRLIF data were taken sequentially along the two diagonal laser injection axes (see Fig. 1) and then synchronized using the transfer functions.

The 2D results are shown in Fig. 19. The discharge current waveform used as the input to the transfer function (Eq. 4) is plotted, along with the time-dependent mean velocity vectors and an example of the IVDFs at one location in the outer beam edge. Non-negligible temporal variations were measured, but the overall amplitude of the oscillations was small. This dataset suggests that oscillations in the beam edges (at least in the $\lesssim 100$ kHz frequency range that was resolved by the measurements) are not likely to be the primary cause of the elevated pole erosion at $V_d = 300$ V.

In the absence of direct validation (e.g., through comparison with another averaging method such as in Fig. 12, which was not possible for these non-periodic oscillations), it is natural to wonder whether the TRLIF results at $V_d = 300$–400 V were physically meaningful. One encouraging piece of evidence is the good correlation between temporal changes in the IVDFs at adjacent velocities, which would not be expected if the time variation predicted by the transfer functions were essentially random. Furthermore, very similar $f(v\,;t)$ results were obtained using the cathode-to-ground voltage $V_{cg}(t)$ rather than the discharge current as the reference waveform. These and other more detailed results from the TRLIF campaign will be presented in an upcoming publication.

V. Conclusion

This paper has presented results from the second LIF campaign on HERMeS TDU-2 at JPL. Following measurements of the acceleration zone properties as a function of operating condition in the first campaign,[8,12] the latest experiments sought to provide insight into remaining questions related to HERMeS life modeling through improved measurement resolution in the spatial and temporal domains. High fidelity time-averaged ion velocity and plasma potential maps were constructed, and time-resolved LIF with ~ 100 kHz bandwidth and good SNR was achieved using the transfer function averaging method. While it requires advanced data acquisition and computing hardware and involves relatively complicated analysis, this approach allows for studies of arbitrary, undriven oscillations in Hall thrusters, making it a powerful tool that should find broader applications now that it has been demonstrated at a second institution following the initial development at the University of Michigan.[21–23]

Acknowledgments

This research was carried out at the Jet Propulsion Laboratory, California Institute of Technology, under a contract with the National Aeronautics and Space Administration. The support of the joint NASA GRC and JPL development of HERMeS by NASA's Space Technology Mission Directorate through the Solar Electric Propulsion Technology Demonstration Mission (SEP TDM) is gratefully acknowledged. We are grateful to Wensheng Huang for sharing the LIF data acquired at NASA GRC and engaging in fruitful discussions about the implications of the results. We would also like to thank Ray Swindlehurst and Nowell Niblett for their assistance in constructing the optical towers, installing the thruster for testing, and maintaining the vacuum facility.

References

[1] R. Hofer, J. Polk, I. Mikellides, A. Lopez Ortega, R. Conversano, V. Chaplin, R. Lobbia, D. Goebel, H. Kamhawi, T. Verhey, G. Williams, J. Mackey, W. Huang, J. Yim, D. Herman, and P. Peterson. Development status of the 12.5 kW Hall Effect Rocket with Magnetic Shielding (HERMeS). In *35th International Electric Propulsion Conference*, Atlanta, GA, October 2017. IEPC-2017-231.

[2]D. A. Herman, T. Tofil, W. Santiago, H. Kamhawi, J. E. Polk, J. S. Snyder, R. R. Hofer, F. Picha, J. Jackson, and M. Allen. Overview of the development and mission application of the Advanced Electric Propulsion System (AEPS). In *35th International Electric Propulsion Conference*, Atlanta, GA, October 2017. IEPC-2017-284.

[3]I. G. Mikellides and I. Katz. Numerical simulations of Hall-effect plasma accelerators on a magnetic-field-aligned-mesh. *Phys. Rev. E*, 86:046703, 2012.

[4]A. Lopez Ortega, I. Mikellides, and V. Chaplin. Hall2De simulations for the assessment of pole erosion in the 12.5 kW Hall Effect Rocket with Magnetic Shielding (HERMeS). In *35th International Electric Propulsion Conference*, Atlanta, GA, October 2017. IEPC-2017-154.

[5]A. Lopez Ortega, I. Mikellides, and D. M. Goebel. Numerical simulations for life assessments of the BaO and LaB_6 cathode options in the Hall Effect Rocket with Magnetic Shielding (HERMeS). In *35th International Electric Propulsion Conference*, Atlanta, GA, October 2017. IEPC-2017-152.

[6]R. A. Stern and J. A. Johnson, III. Plasma ion diagnostics using resonant fluorescence. *Phys. Rev. Lett.*, 34(25):1548–1551, 1975.

[7]R. J. Cedolin, Jr. W. A. Hargus, P. V. Storm, R. K. Hanson, and M. A. Cappelli. Laser-induced fluorescence study of a xenon Hall thruster. *Appl. Phys. B*, 65:459–469, 1997.

[8]V. H. Chaplin, B. A. Jorns, A. Lopez Ortega, I. G. Mikellides, R. W. Conversano, R. B. Lobbia, and R. R. Hofer. Laser-induced fluorescence measurements of acceleration zone scaling in the 12.5 kW HERMeS Hall thruster. *J. Appl. Phys.*, 124:183302, 2018.

[9]N. B. Meezan, W. A. Hargus, and M. A. Cappelli. Anomalous electron mobility in a coaxial Hall discharge plasma. *Phys. Rev. E*, 63:026410, 2001.

[10]A. Lopez Ortega, I. Katz, and V. H. Chaplin. A first-principles model based on saturation of the electron cyclotron drift instability for electron transport in hydrodynamics simulations of Hall thruster plasmas. In *35th International Electric Propulsion Conference*, Atlanta, GA, October 2017. IEPC-2017-178.

[11]A. Lopez Ortega and I. G. Mikellides. Investigations of pole erosion mechanisms in the 12.5 kW HERMeS Hall thruster using numerical simulations and ion velocity measurements. In *54th AIAA/SAE/ASEE Joint Propulsion Conference*, Cincinnati, OH, July 2018. AIAA-2018-4647.

[12]V. H. Chaplin, B. A. Jorns, R. W. Conversano, R. B. Lobbia, A. Lopez Ortega, I .G. Mikellides, and R. R. Hofer. Laser-induced fluorescence measurements of the acceleration zone in the 12.5 kW HERMeS Hall thruster. In *35th International Electric Propulsion Conference*, Atlanta, GA, October 2017. IEPC-2017-229.

[13]W. Huang, H. Kamhawi, and D. A. Herman. Ion velocity in the discharge channel and near-field of the HERMeS Hall thruster. In *54th AIAA/SAE/ASEE Joint Propulsion Conference*, Cincinnati, OH, July 2018. AIAA-2018-4723.

[14]B. A. Jorns, C. Dodson, J. Anderson, D. M. Goebel, R. R. Hofer, M. Sekerak, A. Lopez Ortega, and I. G. Mikellides. Mechanisms for pole piece erosion in a 6-kW magnetically shielded Hall thruster. In *52nd AIAA/SAE/ASEE Joint Propulsion Conference*, Salt Lake City, UT, July 25–27 2016. AIAA-2016-4839.

[15]A. Lopez Ortega, I. G. Mikellides, M. J. Sekerak, and B. A. Jorns. Plasma simulations in 2-D (r-z) geometry for the assessment of pole erosion in a magnetically shielded Hall thruster. *J. Appl. Phys.*, 125:033302, 2019.

[16]I. G. Mikellides, I. Katz, R. R. Hofer, D. M. Goebel, K. de Grys, and A. Mathers. Magnetic shielding of the channel walls in a Hall plasma accelerator. *Phys. Plasmas*, 18:033501, 2011.

[17]R. R. Hofer, D. M. Goebel, I. G. Mikellides, and I. Katz. Magnetic shielding of a laboratory Hall thruster. II. Experiments. *J. Appl. Phys.*, 115:043304, 2014.

[18]I. G. Mikellides, I. Katz, R. R. Hofer, and D. M. Goebel. Magnetic shielding of a laboratory Hall thruster. I. Theory and validation. *J. Appl. Phys.*, 115:043303, 2014.

[19]G. J. Williams, Jr., J. H. Gilland, H. Kamhawi, M. Choi, P. Y. Peterson, and D. Herman. Wear trends of the HERMeS thruster as a function of throttle point. In *35th International Electric Propulsion Conference*, Atlanta, GA, October 2017. IEPC-2017-207.

[20]J. E. Polk, R. B. Lobbia, A. Barriault, V. Chaplin, A. Lopez Ortega, and I. Mikellides. Inner front pole erosion in the 12.5 kW HERMeS Hall thruster over a range of operating conditions. In *35th International Electric Propulsion Conference*, Atlanta, GA, October 2017. IEPC-2017-409.

[21]R. B. Lobbia and A. D. Gallimore. A method of measuring transient plume properties. In *44th AIAA/ASME/SAE/ASEE Joint Propulsion Conference*, Hartford, CT, July 2008. AIAA-2008-4650.

[22]C. J. Durot. *Development of a Time-Resolved Laser-Induced Fluorescence Technique for Nonperiodic Oscillations*. PhD thesis, University of Michigan, 2016.

[23]C. J. Durot, A. D. Gallimore, and T. B. Smith. Validation and evaluation of a novel time-resolved laser-induced fluorescence technique. *Rev. Sci. Instrum.*, 85:013508, 2014.

[24]E. Scime, C. Biloiu, C. Compton, F. Doss, D. Venture, J. Heard, E. Choueiri, and R. Spektor. Laser induced fluorescence in a pulsed argon plasma. *Rev. Sci. Instrum*, 76:026107, 2005.

[25]I. A. Biloiu, X. Sun, and E. E. Scime. High time resolution laser induced fluorescence in pulsed argon plasma. *Rev. Sci. Instrum.*, 77:10F301, 2006.

[26]S. Mazouffre, D. Gawron, and N. Sadeghi. A time-resolved laser induced fluorescence study on the ion velocity distribution function in a Hall thruster after a fast current disruption. *Phys. Plasmas*, 16:043504, 2009.

[27]J. Vaudolon, L. Balika, and S. Mazouffre. Photon counting technique applied to time-resolved laser-induced fluorescence measurements on a stabilized discharge. *Rev. Sci. Instrum.*, 84:073512, 2013.

[28]A. Diallo, S. Keller, Y. Shi, Y. Raitses, and S. Mazouffre. Time-resolved ion velocity distribution in a cylindrical Hall thruster: Heterodyne-based experiment and modeling. *Rev. Sci. Instrum.*, 86:033506, 2015.

[29]N. A. MacDonald, M. A. Cappelli, and W. A. Hargus Jr. Time-synchronized continuous wave laser-induced fluorescence on an oscillatory xenon discharge. *Rev. Sci. Instrum.*, 83:113506, 2012.

[30]N. A. MacDonald, M. A. Cappelli, and W. A. Hargus Jr. Time-synchronized continuous wave laser-induced fluorescence axial velocity measurements in a diverging cusped field thruster. *J. Phys. D: Appl. Phys.*, 47:115204, 2014.

[31]R. B. Lobbia, R. W. Conversano, S. Reilly, R. R. Hofer, and R. Sorensen. Environmental testing of the HERMeS TDU-2 Hall thruster. In *54th AIAA/SAE/ASEE Joint Propulsion Conference*, Cincinnati, OH, July 2018. AIAA-2018-4646.

[32]R. R. Hofer and J. R. Anderson. Finite pressure effects in magnetically shielded Hall thrusters. In *50th AIAA/ASME/SAE/ASEE Joint Propulsion Conference*, Cleveland, OH, July 2014. AIAA-2014-3709.

[33]D. M. Goebel, J. E. Polk, and A. K. Ho. Lanthanum hexaboride hollow cathode performance and wear testing for the Asteroid Redirect Mission Hall thruster. In *52nd AIAA/SAE/ASEE Joint Propulsion Conference*, Salt Lake City, UT, July 2016. AIAA-2016-4835.

[34]R. R. Hofer, B. A. Jorns, I. Katz, and J. R. Brophy. Hall effect thruster electrical configuration. US Patent No. 15/474480, 2017.

[35]V. H. Chaplin, R. W. Conversano, A. Lopez Ortega, I. G. Mikellides, R. B. Lobbia, and R. R. Hofer. Ion velocity measurements in the Magnetically Shielded Miniature Hall Thruster (MaSMi) using laser-induced fluorescence. In *36th International Electric Propulsion Conference*, Vienna, Austria, September 2019. IEPC-2019-531.

[36]W. Huang. *Study of Hall Thruster Discharge Channel Wall Erosion via Optical Diagnostics*. PhD thesis, University of Michigan, 2011.

[37]D. J. Gershman, J. C. Dorelli, A. F-Vinas, and C. J. Pollock. The calculation of moment uncertainties from velocity distribution functions with random errors. *J. Geophys. Res.-Space Phys.*, 120(8):6633–6645, 2015.

[38]B. Efron. Bootstrap methods - Another look at the jackknife. *Ann. Stat.*, 7(1):1–26, 1979.

[39]G. Paschmann and P. W. Daly. Analysis methods for multi-spacecraft data. Technical Report SR-001, International Space Science Institute, 1998.

[40]R. Hofer, J. Polk, M. Sekerak, I. Mikellides, H. Kamhawi, T. Verhey, D. Herman, and G. Williams. The 12.5 kW Hall Effect Rocket with Magnetic Shielding (HERMeS) for the Asteroid Redirect Robotic Mission. In *52nd AIAA/SAE/ASEE Joint Propulsion Conference*, Salt Lake City, UT, July 2016. AIAA-2016-4825.

[41]J. D. Frieman, H. Kamhawi, G. Williams, D. Herman, P. Y. Peterson, J. Gilland, and R. Hofer. Long duration wear test of the NASA HERMeS Hall thruster. In *54th AIAA/SAE/ASEE Joint Propulsion Conference*, Cincinnati, OH, July 2018. AIAA-2018-4645.

[42]I. G. Mikellides, I. Katz, R. R. Hofer, and D. M. Goebel. Magnetic shielding of walls from the unmagnetized ion beam in a Hall thruster. *Appl. Phys. Lett.*, 102:023509, 2013.

[43]I. G. Mikellides and I. Katz. Wear mechanisms in electron sources for ion propulsion I: Neutralizer hollow cathode. *J. Propul. Power*, 24(4):855–865, 2008.

[44]I. G. Mikellides and I. Katz. Wear mechanisms in electron sources for ion propulsion II: Discharge hollow cathode. *J. Propul. Power*, 24(4):866–879, 2008.

[45]I. G. Mikellides, I. Katz, D. M. Goebel, and K. K. Jameson. Evidence of nonclassical plasma transport in hollow cathodes for electric propulsion. *J. Appl. Phys.*, 101:063301, 2007.

[46]J. T. Yim. A survey of xenon ion sputter yield data and fits relevant to electric propulsion spacecraft integration. In *35th International Electric Propulsion Conference*, Atlanta, GA, October 2017. IEPC-2017-060.

[47]I. G. Mikellides and A. Lopez Ortega. Assessment of pole erosion in a magnetically shielded Hall thruster. In *50th Joint Propulsion Conference*, Cleveland, OH, July 2014. AIAA-2014-3897.

[48]M. S. McDonald and A. D. Gallimore. Rotating spoke instabilities in Hall thrusters. *IEEE Trans. Plasma Sci.*, 39(11):2952–2953, 2011.

[49]S. Barral and E. Ahedo. Low-frequency model of breathing oscillations in Hall discharges. *Phys. Rev. E*, 79:046401, 2009.